remote sensing

MDPI

Article

A Multi-Level Semi-Automatic Procedure for the Monitoring of Bridges in Road Infrastructure Using MT-DInSAR Data

Diego Alejandro Talledo * and Anna Saetta

Department of Architecture and Arts, University IUAV of Venezia, Dorsoduro 2206, 30123 Venezia, Italy; anna.saetta@iuav.it

* Correspondence: diego.talledo@iuav.it

Abstract

Monitoring the structural health of bridges in road infrastructure is crucial for ensuring public safety and efficient maintenance. This paper presents a multi-level semi-automatic methodology for bridge monitoring, using Multi-Temporal Differential SAR Interferometry (MT-DInSAR) data. The proposed approach requires a dataset of satellite-derived MT-DInSAR measurements for the Area of Interest. The methodology involves creating a georeferenced database of bridges which allows the filtering of measurement points (generally named Persistent Scatterers—PSs) using spatial queries. Since existing datasets often provide only point geometries for bridge locations, additional data sources such as OpenStreetMaps-derived repositories have been utilized to obtain linear representations of bridges. These linear features are segmented into 20 m sections, which are then converted into polygonal geometries by applying a uniform buffer. Spatial joining between the bridge polygons and PS datasets allows the extraction of key statistics, such as mean displacement velocity, PS density and coherence levels. Based on predefined velocity thresholds, warning flags are triggered, indicating the need for further in-depth analysis. Finally, an upscaling step is performed to provide a practical tool for infrastructure managers, visually categorizing bridges based on the presence of flagged pixels. The proposed approach facilitates large-scale bridge monitoring, supporting the early detection of potential structural issues.

Keywords: MT-DInSAR data; infrastructures; monitoring; bridges; warning flags

Academic Editor: Wen Liu

Received: 12 May 2025
Revised: 26 June 2025
Accepted: 4 July 2025
Published: 10 July 2025

Citation: Talledo, D.A.; Saetta, A. A Multi-Level Semi-Automatic Procedure for the Monitoring of Bridges in Road Infrastructure Using MT-DInSAR Data. *Remote Sens.* **2025**, *17*, 2377. https://doi.org/10.3390/rs17142377

1. Introduction

The continuous monitoring of bridge infrastructure is critical to safeguarding transportation networks and ensuring public safety. Bridges, subjected to increasing traffic loads, environmental degradation and material aging, are prone to various deterioration mechanisms that, if undetected, may compromise structural integrity. Conventional monitoring techniques, such as periodic visual inspections and localized in situ instrumentation, although widely adopted and effective for detecting a number of damage types, present significant limitations in terms of difficulties in installation, spatial coverage, operational costs and sensitivity to early-stage deformations that might underlie a structural problem. These constraints underscore the need for advanced, scalable and more efficient monitoring approaches.

Remote sensing technologies, particularly satellite-based Interferometric Synthetic Aperture Radar (InSAR), have revolutionized the field of structural health monitoring over the past two decades. InSAR enables the non-contact, high-precision measurement of surface and structural displacements over wide geographic areas, enabling the detection of

millimetric-scale displacements independent of ground accessibility or lighting conditions. Within the InSAR framework, multi-temporal techniques (MT-InSAR), such as Persistent Scatterer (PS-InSAR) and Small Baseline Subset (SBAS) methods, have been extensively validated for their ability to detect subtle deformation patterns associated with processes like ground subsidence, landslides and other geo-hazards [1–4]. Such capabilities position MT-InSAR as a powerful complement to traditional inspection methods, particularly in the early detection of structural vulnerabilities.

Recent technological advancements have further enhanced the potential applicability of InSAR for infrastructure monitoring. The proliferation of new satellite missions—including high-resolution constellations like TerraSAR-X, COSMO-SkyMed and the more recent Capella Space and ICEYE platforms—provides increased spatial and temporal resolution, allowing for more frequent observations and finer-scale deformation analysis. Moreover, the availability of data across multiple radar frequencies (e.g., X-, C- and L-bands) enables tailored monitoring strategies depending on the structural characteristics and environmental conditions. These developments, combined with improved processing algorithms leveraging machine learning and cloud computing resources, are paving the way for near-real-time deformation monitoring, dramatically expanding the potential for early warning systems and proactive maintenance planning.

In this evolving context, MT-InSAR is increasingly recognized not merely as a complementary tool to traditional inspections but as a cornerstone of integrated, data-driven bridge management strategies.

While some applications are mainly focused on isolated infrastructure segments and retrospective failure assessments [5–7], recent research has shifted towards more proactive and large-scale monitoring approaches. For example, refs. [8,9] demonstrated the potential of fully automated InSAR-based systems for the nationwide monitoring of road and railway networks. Similarly, studies have proposed early-warning frameworks for detecting anomalies in bridge behavior [10–12].

The scientific community has responded to these advancements with an exponential growth in publications and conference sessions on InSAR-based structural health monitoring (SHM), reflecting its rising relevance in civil engineering [13].

Bridges, in particular, have become a focal point in recent investigations. Multiple validation strategies have been employed to enhance the reliability of InSAR-derived displacements. For instance, ref. [14] compared PS-InSAR measurements with terrestrial LiDAR data to track long-span bridge deflections. Ref. [15] linked seasonal thermal effects to girder deformations using TerraSAR-X imagery, while [16] applied D-TomoSAR techniques to Sentinel-1 data, achieving high accuracy in displacement detection. In a more tailored approach, ref. [17] developed a post-processing methodology specifically designed for multi-span bridges, emphasizing the role of uncertainty quantification in infrastructure risk assessment. More recently, ref. [18] introduced a satellite-based DInSAR approach for large-scale bridge network monitoring, enabling risk classification by analyzing deformation patterns at both territorial and local scales, showing an application on an Italian road artery near Naples including 68 bridges.

As previously mentioned, recently launched commercial satellite constellations such as ICEYE and Capella [19,20] are capable of delivering data with sub-meter spatial resolution and revisit times as short as one hour, offering the potential for near-real-time monitoring [21]. Preliminary studies have demonstrated the potential of such new constellations; for instance, ref. [22] shows the use of ICEYE data for the analysis of slope failures, while ref. [23] presents various use cases and highlights the advanced capabilities of the Capella constellation.

Regarding bridge monitoring, ref. [24] emphasizes for railway bridges that advancements in satellite technology—particularly the deployment of high-temporal-resolution constellations such as ICEYE and Capella Space—can help overcome the challenges associated with limited revisit intervals. Integrating satellite observations with ground-based IoT sensor networks offers a synergistic solution that enhances both spatial coverage and temporal resolution, paving the way for near-real-time surveillance and data-driven predictive maintenance strategies.

Finally, cloud-based frameworks for Interferometric Synthetic Aperture Radar (InSAR) time-series processing are showing great promise. For example, ref. [25] showcases the scalability of cloud computing approaches for generating interferograms and the use of advanced processing tools to analyze time-series data over extensive and tectonically active regions.

In this study, starting and extending a similar approach previously proposed by the authors for the monitoring of historical buildings [26], we propose a semi-automatic multi-level methodology that leverages MT-DInSAR data for large-scale bridge monitoring. The proposed approach may utilize satellite datasets processed with specific algorithms (e.g., SBAS as well as PS techniques) to generate displacement measurements. However, to effectively analyze bridge-specific deformations, it is necessary to associate PS data with accurate bridge geometries in a Geographic Information System (GIS) environment.

This paper focuses on overcoming the limitations of existing bridge datasets by integrating OpenStreetMap-derived repositories to obtain linear representations of bridges, which are then transformed into polygons to facilitate spatial queries. The final goal is to propose a methodology to automate the identification of bridges exhibiting significant deformation trends and provide actionable insights for infrastructure managers.

Finally, the proposed procedure is applied to a network of bridges located along a transport corridor between Tirano and Marghera, designated for exceptional transport operations, analyzed as one of the Proofs of Concept (referred as POC2) [27] in the framework of the National Recovery and Resilience Plan (NRRP) RETURN project, Spoke TS2.

2. Proposed Methodology

2.1. Workflow

The methodology proposed is schematically illustrated in the workflow of Figure 1 and is briefly outlined in this section. The first step requires the identification of the infrastructure network of interest (referred to as the Area of Interest, AOI). Two key datasets are then required for the AOI, described in more detail in Section 2.2:

1. A satellite data dataset in the AOI.
   The monitoring process relies on Multi-Temporal Differential Interferometric Synthetic Aperture Radar (MT-DInSAR) analysis. Different satellite data can be adopted. Among the most commonly used datasets, the data from the Sentinel constellation processed and made available by the European Ground Motion Service (EGMS) are well-suited for broad-scale applications, while, for example, data from the first- and second-generation COSMO-SkyMed (CSK) constellations are more effective when applied to smaller, localized areas.
2. A georeferenced database of bridges in the AOI.
   The proposed methodology requires the availability of polygons representing bridges in order to enable spatial queries and the filtering of measurement points (also named as PSs, Persistent Scatterers). However, existing datasets often only provide point geometries indicating bridge locations (latitude and longitude coordinates) within Geographic Information System (GIS) environments, thus requiring additional processing to determine bridge lengths and, subsequently, potential widths.

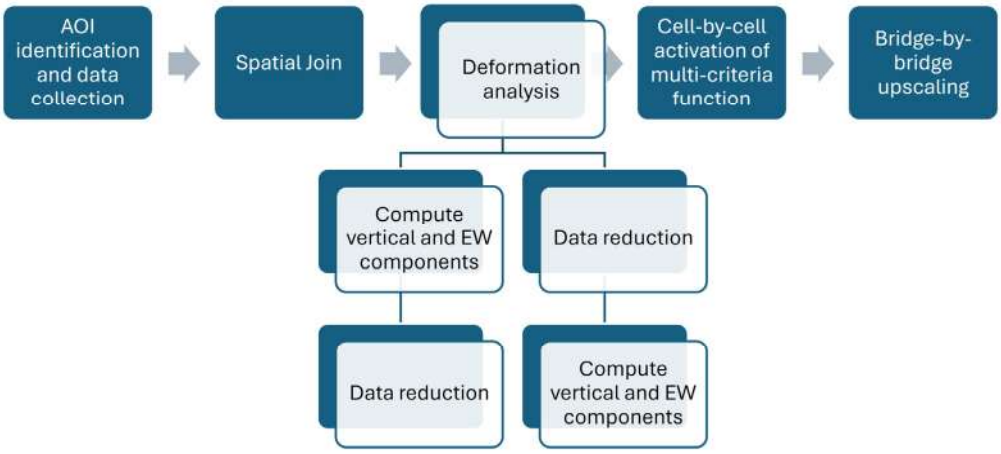

Figure 1. Workflow of proposed methodology.

The following step requires a spatial join operation, which is described in Section 2.3. Such a spatial join shall be performed between the polygonal pixels of the bridges and the PS datasets.

Starting from the spatial join, two different alternative approaches can be adopted to compute the mean vertical and horizontal east–west velocities for each grid cell, depending on the order in which the two operations—"combining ascending and descending datasets" and "data reduction"—are carried out. Furthermore, the method for selecting the datasets to be combined, when more than one is available, must be defined.

Finally, the methodology includes an alert system and an upscaling phase, which are described in detail in Section 2.4.

2.2. Key Datasets

2.2.1. Satellite Data

The proposed methodology can be implemented using different types of satellite data. In the following example, the EGMS dataset is adopted for applying the methodology to the whole AOI. It is worth noting that for smaller, localized areas, CSK data can be effectively used to enhance the resolution and, consequently, the level of reliability required when analyzing at the scale of individual structures.

The EGMS is an Earth observation product under the Copernicus Land Monitoring Service, implemented by the European Environment Agency. It provides consistent, millimeter-precision measurements of ground deformation across Europe (see Figure 2) by processing imagery from the Sentinel-1 satellite constellation. The EGMS has been operational since late 2022 and delivers open-access InSAR datasets derived from Sentinel-1 data acquired from 2015 onward [28–30]. Data are generated using multi-temporal SAR interferometry techniques (specifically Persistent Scatterer Interferometry, PSI, and quasi-PSI methods such as SqueeSAR [2]) which identify stable reflectors (which are the previously defined Persistent Scatterers, PSs, or measure points) on the ground and track their motion over time. This approach enables the detection of small structural displacements in the order of a few millimeters.

Sentinel-1A and -1B, launched in 2014 and 2016, respectively, form a twin C-band SAR satellite constellation in sun-synchronous near-polar orbit. The two satellites are phased 180° apart, allowing a combined revisit time of about 6 days. Each Sentinel-1 satellite operates primarily in Interferometric Wide (IW) swath mode over land, achieving a ground resolution of the order of about 5 m (range direction) by 20 m (azimuth direction) with a 250 km swath. This relatively high spatial resolution and frequent repeat interval, together with the open and free nature of its data, make Sentinel-1 well-suited for the

interferometric monitoring of large-scale ground and structural movements. Furthermore, its radar instrumentation permits acquisitions independent of daylight or weather, ensuring a continuous data record. The EGMS capitalizes on these capabilities by systematically processing Sentinel-1 IW SAR images to produce standardized deformation measurements across Europe.

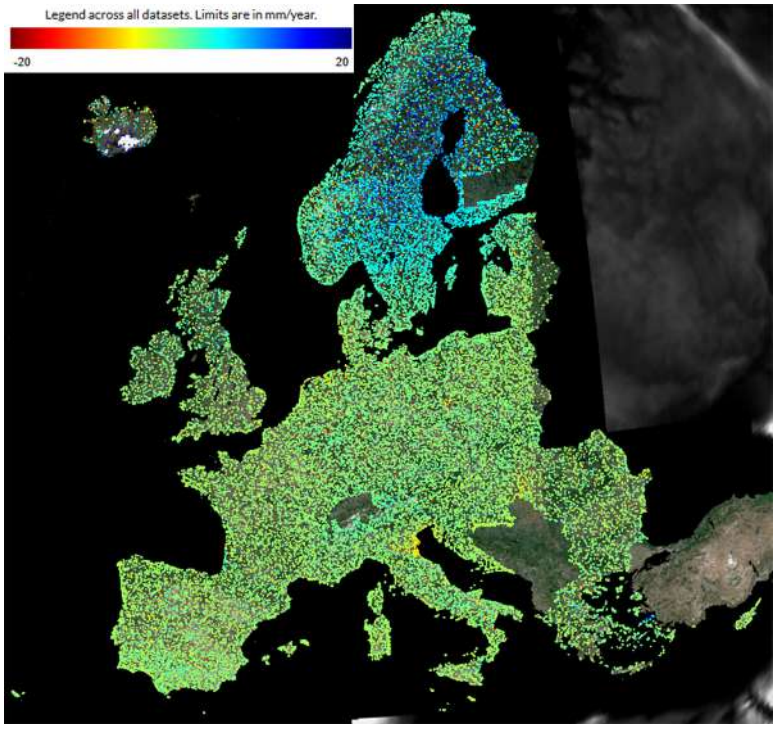

Figure 2. Overview of available EGMS data.

The EGMS provides three levels of InSAR-derived ground motion products (all obtained from Sentinel-1 imagery) for user access [28–30]:

- Basic (Level 2a): This provides displacement measurements along the satellite Line of Sight (LOS) for single data tiles with respect to a local virtual reference point located within each data tile. This means that every data tile has its own reference point, making the velocities and displacement measures relative. It contains geo-localization information (both in plan and in elevation), temporal coherence, displacement velocity (both mean and standard deviation), acceleration (both mean and standard deviation) and seasonal component (both mean and standard deviation), together with the full time series of displacement for each PS. The full resolution (i.e., about 5 × 20 m) of the Sentinel sensor is exploited. The product is delivered as separate datasets for the different tracks and for both ascending and descending orbit geometries.
- Calibrated (Level 2b): This provides data corrected using a GNSS-based deformation model, thereby making all the displacement measures absolute (referenced to an Earth-centered datum). This product contains the same information as the Basic one and exploits the full resolution of the Sentinel sensor of about 5 × 20 m. In this case the product is delivered as separate datasets for ascending and descending orbit geometries.
- Ortho (Level 3): Starting from ascending and descending L2b (i.e., calibrated) products, these data are combined to solve for mean vertical and horizontal east–west velocities at each location. To achieve this result, the ascending and descending L2b datasets are down-sampled to a regular 100 m × 100 m grid. The resulting L3 dataset provides the time series and velocities of ground motion in standard geographic directions,

which can be easier to interpret for large-scale ground stability assessment. Ortho products are anchored to the GNSS reference frame (i.e., the measures are absolute) and are organized in 100 km × 100 km tiles for dissemination. Unfortunately, due to the poor spatial resolution, this product cannot be used generally for structural health monitoring, even at territorial scale.

For the purposes of this study, which focuses on local-scale deformation analysis along an infrastructure network, the EGMS Basic (L2a) product was selected as the primary data source for satellite data. The Basic product is the suggested product by the EGMS for the analysis of buildings and structures in general, characterized by local deformation phenomena [31], and preserving the highest spatial density of measurement points is a key aspect for monitoring structures.

Concerning the temporal coverage, the EGMS adopts a rolling multi-year monitoring strategy with the release of annual updates. Except for the initial release (published in 2022) covering the period 2015–2021, the subsequent releases consider five-year moving windows. Therefore, in 2023 the second release covering the period 2018–2022 was published, while in 2024 the product released covered the period 2019–2023. During 2025, the publishing of the fourth release covering the period 2020–2024 is expected. In the EGMS viewer the most recent product is visualized, while users can also always download previous releases. This strategy of the EGMS is particularly interesting because it allows the definition of warning-activation criteria when the measurements for the current release depart from the measurements of the previous releases.

To integrate the EGMS satellite data into the analysis framework, a dedicated data collection process consisting of a specific processing workflow was followed. The workflow consisted of four main steps: Data Retrieval, Dataset Assembly, Data Export and Conversion, and AOI Clipping. Each step is described and explained in detail below. All the steps were performed using the open-source EGMS-toolkit (version 0.2.15 Beta, Apr., 2025) [32] (a Python-based (version 3.10.5) API and toolset for EGMS data) and GDAL (version 3.10.3) [33] (a translator library for raster and vector geospatial data), and standard GIS software (opensource QGIS software (version 3.34.2)) was used in this work.

Data Retrieval: The first step involves the retrieval of the necessary satellite dataset; this was performed by programmatically querying and downloading the EGMS Basic (L2a) datasets for the selected study area (AOI) using the EGMS-toolkit Python API.

Using the toolkit, all ascending and descending orbit tracks covering the AOI were identified, and all relevant Sentinel-1 burst datasets were obtained (in the EGMS, each data file corresponds to a single Sentinel-1 IW burst within a given track and frame.) This ensured the full coverage of the AOI from both viewing geometries. This was performed for all the time windows available in the EGMS server (i.e., 2015–2021, 2018–2022, 2019–2023).

Dataset Assembly: The raw EGMS files from multiple bursts and frames were then combined using the EGMS-toolkit API. All burst-level point datasets for each orbit direction (ascending and descending) and track were merged to produce continuous point clouds covering the entire AOI. During this merging, overlapping points arising from adjacent burst boundaries were identified as duplicates and removed [32]. This step prevents the double-counting of the same measurement point which might appear in two neighboring burst files. After merging, the result was a unified set of unique PSs for the AOI in each geometry, with associated time series and mean displacement velocities.

Data Export and Conversion: The merged point datasets (one per geometry) were exported from EGMS-toolkit in the comma-separated value (CSV) format, containing columns for point coordinates, mean velocities, time-series parameters and quality metrics. For more efficient spatial analysis, the CSV data was converted into a geospatial database format using the GDAL tool ogr2ogr. In particular, the data were converted into a GeoPackage

(GPKG)—an open standard single-file GIS database. This conversion involved assigning the appropriate coordinate reference system (ETRS89/LAEA Europe, EPSG:3035, as used by EGMS products) and creating spatial index structures on the point data. The use of a GPKG with spatial indexing greatly improved performance in subsequent queries, visualization and spatial joins, especially given the large number of measurement points (that can be even in the order of hundreds of thousands up to millions for large AOIs).

AOI Clipping: Finally, the geospatial dataset was clipped to the exact AOI boundaries. Although the initial download was restricted to the general vicinity of the AOI, clipping ensured that any points lying outside the buffer (e.g., the data downloaded if a burst partially overlapped the AOI) were excluded from the analysis. The final result was a clean point set of EGMS Basic measurements strictly within the AOI. This dataset—containing both ascending and descending data points for the different analyzed tracks—forms the basis for the following spatial join and deformation analysis, providing time-series displacement information for each Persistent Scatterer on or near the structures.

All the above steps were conducted in a systematic, automated manner to minimize human error and ensure reproducibility. The use of EGMS-toolkit, together with command line GDAL tools, allowed us to seamlessly handle the large volume of satellite data and perform the necessary post-processing (merging, filtering, clipping) within a unified workflow. The processed EGMS Basic dataset was then ready for integration into the subsequent analysis phases, such as identifying deformation trends, correlating with structural features and validating against ground-based observations (as detailed in later sections of this paper). By leveraging the Copernicus EGMS data and this processing approach, we established a robust satellite-based data foundation for the structural health monitoring framework.

2.2.2. Bridges Dataset

To enhance spatial representation, additional data sources can be used to derive at least the linear extent of bridges (resulting in line geometries in the GIS) or, preferably, the complete footprint of bridge decks (corresponding to polygon geometries in the GIS). While the latter is preferable, it is not always readily available. In some cases, databases contain only a single point representing a bridge's location. This heterogeneity of data in the available datasets requires the preliminary processing of bridge databases that must be carried out before proceeding with the subsequent steps of the procedure.

Different repositories can be used for obtaining information about bridges belonging to a selected AOI. Among others, a very effective one is the open-data repository created by the OpenData SiciliaHub community based on OpenStreetMap data [34], containing georeferenced data for all the bridges in Italy, categorized by region. The dataset includes all types of bridges—highway, road and pedestrian/cycling bridges—represented as linear features.

As an example, Figure 3 illustrates the bridges located in northeast Italy, with a zoomed-in view of Venice, where it can be verified that the dataset includes not only road and railway bridges, but also all pedestrian ones.

When the geo-dataset comprises surface geometries representing the decks of the bridges, the polygons can be discretized into pixels in order to apply the proposed procedure. When the geo-dataset instead represents bridges as single-point geometries, a surface or at least a linear geometry for each bridge must be created. If the AOI is limited with a relatively small number of bridges, this operation can be performed manually using ancillary data that can be obtained (e.g., ortho-photo, technical charts, satellite optical data, etc.). On the other hand, when the AOI is large and includes a high number of bridges, the operation can be performed automatically by means of spatial joining with a database including linear geometries like the one above mentioned based on OpenStreetMaps.

(**a**) (**b**)

Figure 3. Representation of bridge dataset: (**a**) Overview of bridges in northeast Italy; (**b**) zoomed-in view of Venice area (highlighted with red square in (**a**)).

Finally, if the geo-dataset represents the bridges as linear geometries, an algorithmic procedure must be applied to convert these lines into a set of regular grids or pixels corresponding to the different bridges. Specifically, in this study, each bridge line (shown in yellow in Figure 3) was segmented into sections with a maximum length of 20 m, enabling the reliable assessment of the deformation distribution along the bridges.

It is worth noting that the maximum length should be chosen accounting for the satellite data considered, with particular reference to the resolution and the geo-localization precision. Then, to transform the linear bridge geometries into pixel-shaped polygons, a constant-width buffer should be applied. This approach, although a simplification, provides an approximation of the bridge deck width, which typically varies among different structures. It is worth noting that this dimension should also account for the resolution and positional uncertainty of the satellite dataset used. In this study, a buffer width of 10 m was chosen, resulting in polygon pixels with a total cell size of 20 m for subsampling PS measurements in the subsequent phases. Depending on the resolution of the available satellite data (e.g., CSK vs. Sentinel-1) and the monitoring scale, different criteria could be adopted for defining the buffer width. Since this study focused on methodological development by using EGMS dataset, a 20 m width was selected as it aligned better with the Sentinel-1 system's spatial resolution.

Following this processing step, the dataset consists of rectangular grid cells (or pixels) subdividing each bridge, as illustrated in Figure 4 for a sample area including two bridges, one per direction of travel.

2.3. Spatial Join and Deformation Analysis

Once the bridge dataset has been structured, a spatial join is performed between the polygonal pixels of the bridges and the PS dataset. This operation enables the extraction of key statistical indicators of the PS points falling within each grid cell, including

- The number and density of PS points;
- The mean coherence of the PS points;
- The mean and standard deviation of the LOS velocities;
- The mean time series of displacement.

During this process, additional filtering criteria can be applied to refine the selection of measurement points. For example, filters based on coherence thresholds or elevation values can be used to ensure that only PS points belonging to bridge decks are considered. However, at a large scale, such filtering is not trivial and was not applied in this study, meaning that all the available PS points within the grid cells were included.

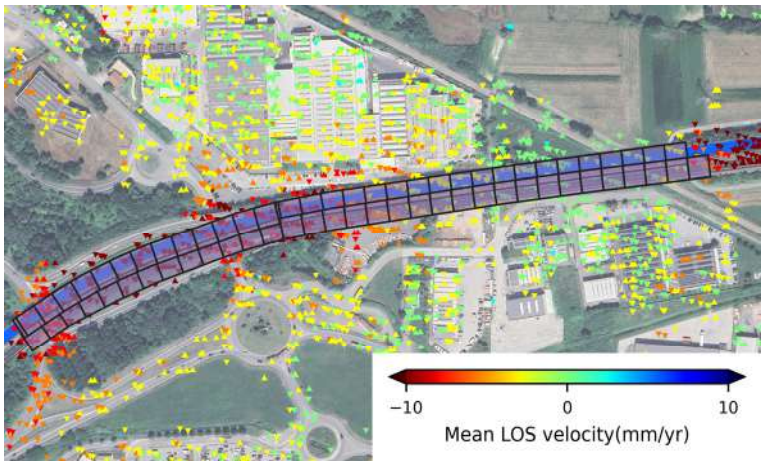

Figure 4. View of two bridges (one per direction of travel) in sample area, segmented into rectangular sections. Ascending (up-pointing triangles) and descending (down-pointing triangles) PSs for time window 2015–2021 superimposed.

It is worth noting that usually the north–south component is assumed as zero since the sensitivity of the satellite sensor to that direction is very small. The vertical and horizontal east–west components can be derived by combining one ascending and one descending acquisition using LOS velocity and the corresponding LOS direction cosines. This is obtained by solving the following system written in matrix form:

$$\begin{bmatrix} v_{LOS}^{A} \\ v_{LOS}^{D} \end{bmatrix} = \begin{bmatrix} c_{E}^{A} & c_{U}^{A} \\ c_{E}^{D} & c_{U}^{D} \end{bmatrix} \cdot \begin{bmatrix} v_{E} \\ v_{U} \end{bmatrix} \quad (1)$$

where v_{LOS}^{A} and v_{LOS}^{D} are the mean velocities along the LOS for the ascending and descending orbits, respectively; v_E is the east–west mean velocity; v_U is the mean vertical velocity; and c_E^A, c_U^A, c_E^D and c_U^D are the east and vertical cosine directors of the LOS for the ascending and descending orbits.

As anticipated in Section 2.1, two different approaches can be adopted to compute the mean vertical and horizontal east–west velocities for each grid cell, depending on the order in which the two operations—"combining ascending and descending datasets" and "data reduction"—are carried out. Specifically, two possible approaches can be followed.

Left-Hand Path (as indicated in the workflow in Figure 1): According to this approach, each available ascending dataset is combined with each available descending dataset to obtain the mean vertical and horizontal east–west velocity values for each cell (taking into account the various possibilities provided by the availability of ascending and descending datasets, which can range from zero to two per type, e.g., ASC1, ASC2, DES1, DES2). Then, a data reduction process is performed to yield a single mean vertical velocity value and one mean horizontal east–west velocity value. For example, this can be achieved by selecting the maximum vertical value and the corresponding horizontal east–west value. This operation can be executed on a pixel-by-pixel basis; however, this may lead to a situation where different pixels within the same bridge have values derived from different dataset combinations (e.g., one pixel has a value obtained from combining ASC1 and DES1 while another from ASC1 and DES2). Alternatively, a bridge-by-bridge evaluation can be conducted by maintaining consistent dataset combinations for all pixels within the same bridge—that is, for the same bridge, all mean vertical and horizontal east–west velocity values are derived from the same two datasets.

It should be noted that, in theory, significant differences in mean vertical and horizontal east–west velocities should not occur in overlapping zones.

Right-Hand Path (as indicated in the workflow in Figure 1): According to this approach, a data reduction process is executed by choosing one ascending and one descending dataset. This can again be performed either on a pixel-by-pixel basis or on a bridge-by-bridge basis. The key here is to make the selection based on parameters obtained from data statistics (e.g., mean coherence, number of points). At this point, a single ascending and a single descending track are selected, along with their mean vertical and horizontal east–west component values.

It is worth noting that a further possibility could be considered: the use of all available datasets for ascending and descending geometries combined together to solve the system and derive the velocity/displacement components. Some preliminary tests using this approach showed encouraging results, even if more tests remain necessary to define a good strategy for solving the system: Ordinary Least Squares considers all the available tracks equally, while Weighted Least Squares can be used for weighting more reliable tracks.

At the end of the process, it is possible to visualize deformation trends along the bridge, as shown in Figure 5 for the previously defined sample area, where the mean velocities for ascending orbit for the time window 2015–2021 are mapped to identify potential areas of concern.

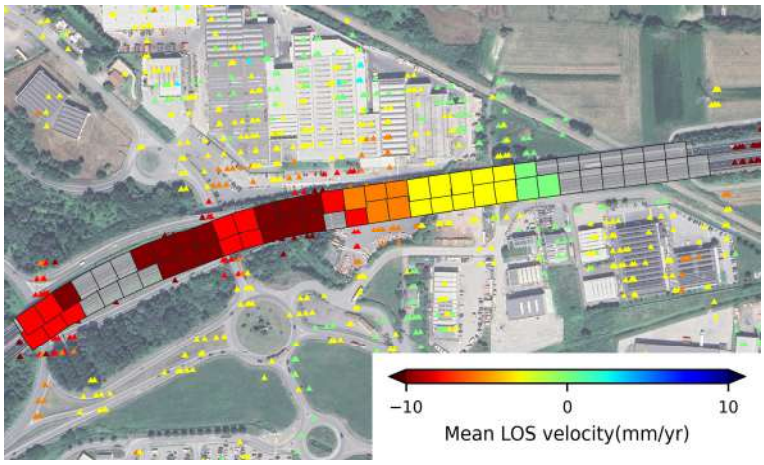

Figure 5. A map of mean velocity for a sample area for ascending orbit and the time window 2015–2021. Ascending PSs (up-pointing triangles) for the same time window are superimposed. The transparent pixels denote portions where ascending dataset information is not available.

2.4. Alert System and Upscaling

The alert system for bridge monitoring is based on a multi-criteria framework applied to each grid cell. This system integrates multiple displacement indicators, including mean vertical and horizontal east–west velocities as well as ascending and descending mean velocities. An effective warning is triggered, for example, when the computed mean vertical or horizontal east–west velocity exceeds a predefined threshold within any pixel of the bridge. This threshold serves as an early indicator for potential structural instabilities, prompting further investigation with higher-resolution monitoring techniques tailored to the scale of the individual bridge.

To enhance the robustness of the alert system, statistical measures are incorporated to assess the reliability of the computed velocity estimates and to evaluate spatial consistency among adjacent grid cells that are part of the same bridge. One key parameter considered is the Standard Error of the Mean (SEM), defined as, per ref. [35],

$$SEM = \sqrt{\frac{1}{N^2}\sum_{i=1}^{N}\sigma_i^2} \quad (2)$$

where σ_i is the standard deviation of the velocity of the *i-th* PS within the cell and N is the number of PS points contained in the cell. The *SEM* provides a quantitative measure of the uncertainty associated with the estimated mean displacement velocity, ensuring that grid cells with a limited number of points are appropriately weighted in the analysis. Furthermore, confidence intervals for the mean displacement velocity can be computed based on the *SEM*, allowing for an estimation of the range within which the true mean displacement velocity is expected to fall with a given level of confidence.

This information can also be used for estimating the uncertainty of vertical and east–west mean velocities. System (1) can be rewritten in compact matrix form:

$$\boldsymbol{v}_{LOS} = \mathbf{A} \cdot \mathbf{v} \tag{3}$$

And the solution of the vertical and east–west components is simply

$$\mathbf{v} = \mathbf{A}^{-1} \cdot \boldsymbol{v}_{LOS} \tag{4}$$

Assuming the uncertainties along the LOS for the ascending and descending orbits are uncorrelated, in line with other studies, e.g., refs. [17,36], their covariance matrix is diagonal:

$$\boldsymbol{\Sigma}_{LOS} = \begin{bmatrix} SEM_A^2 & 0 \\ 0 & SEM_D^2 \end{bmatrix} \tag{5}$$

The propagation of uncertainty through the linear system permits us to obtain the covariance matrix for the vertical and east–west components $\boldsymbol{\Sigma}_{V,EW}$ as follows:

$$\boldsymbol{\Sigma}_{V,EW} = \boldsymbol{A}^{-1} \cdot \boldsymbol{\Sigma}_{LOS} \cdot \left(\boldsymbol{A}^{-1}\right)^T \tag{6}$$

Finally, the uncertainty of the vertical and east–west components can be determined

$$\begin{aligned} \sigma_{V_{EW}} &= \sqrt{(\Sigma_{V,EW})_{11}} \\ \sigma_{V_U} &= \sqrt{(\Sigma_{V,EW})_{22}} \end{aligned} \tag{7}$$

By integrating these statistical approaches, the alert system achieves a higher level of reliability, ensuring that warnings are based not only on deterministic displacement values but also on the statistical robustness of the observations.

To facilitate decision-making for infrastructure managers, an upscaling procedure is introduced. A bridge is classified as critical if at least one of its pixels contains an active warning flag. This method enables the rapid identification of structures requiring further inspection, thereby supporting proactive maintenance strategies and mitigating the risk of structural failures.

3. Case Study: Definition of AOI and Data Collection

The case study concerned the transport corridor connecting the Swiss border (Tirano) with Maghera port, passing through Milano and under investigation as Proof of Concept number 2 (referred as POC2) within the Return project in the framework of the NRRP [27].

The proposed methodology was applied to the whole corridor using datasets obtained from the European Ground Motion Service (EGMS) within the Copernicus framework as satellite data.

The corridor was selected to ensure the safe transit of the exceptional transports that are significantly growing in the northeast of Italy. Five alternative routes to the main one were selected in the project. The corridor traverses two Italian regions, Lombardy and

Veneto, and encompasses various types of roadways, ranging from minor urban streets to state and provincial roads. It is important to note that highways were excluded from the corridor, as the transit of Heavy Goods Vehicles (HGVs) is prohibited on these routes.

A total of almost 300 bridges were included along the corridor (including the alternative routes), featuring a wide variety of structural types and construction materials. In terms of materials, the bridges are made of concrete, masonry and steel, while the main structural typologies include arches, caissons, slabs, simply supported beams, continuous beams and Gerber beams. Moreover, the total bridge lengths varied significantly, ranging from a minimum of approximately a few meters up to hundreds of meters. Correspondingly, the number of spans extended from a single span to about 10 spans.

The majority of the bridges span watercourses—although only a few cross major rivers with significant flow, with most structures passing over small streams or drainage channels. Approximately one-third of the bridges are road overpasses, whereas the remaining structures either span railway lines or feature mixed crossings. The latter include combinations such as road and river crossings, river and railway crossings, railway and road crossings or even crossings involving all three—river, railway and road simultaneously. Finally, a small number of bridges did not span any crossings but were instead constructed to overcome natural topographic discontinuities [27].

Concerning the Data Retrieval described in Section 2.2.1, the Area of Interest (AOI) of the case study was defined as the corridor encompassing the POC2 path (the monitored structure's path) with a 1 km buffer on either side, see Figure 6. Each bridge belonging to the POC2 corridor had a progressive identifier, referred to in this paper as POC2-IDn, with n the progressive number of the bridge.

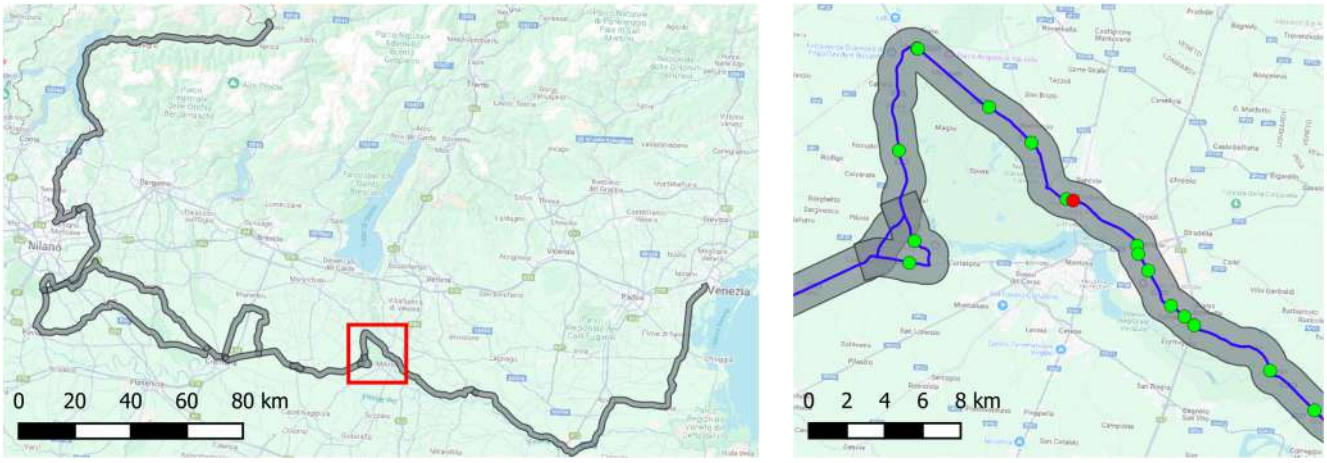

(**a**) (**b**)

Figure 6. AOI selected for downloading and processing EGMS data: (**a**) view of whole AOI, (**b**) zoom-in on red squared portion of AOI near Mantova showing POC2 corridor (blue line), bridges of POC2 corridor (green dots), case study bridge POC2-ID6 (red point) and 1 km buffer (gray shaded area) selected as AOI.

This buffered AOI polygon was used to filter EGMS data to only those points sufficiently near the structure. As stated in Section 2.2.1, using EGMS-toolkit, all ascending and descending orbit tracks covering the AOI were identified, and all relevant Sentinel-1 burst datasets were obtained for the three time windows available on the EGMS servers (i.e., 2015–2021, 2018–2022, 2019–2023). Figure 7a,b show, respectively, the ascending and descending bursts individuated and downloaded for each time window. Specifically, 22 bursts for the ascending dataset including tracks 015, 044 and 117 were downloaded,

while 27 bursts for the descending dataset including tracks 066, 095 and 168 were downloaded. In Figure 7 the different tracks are represented with different colors.

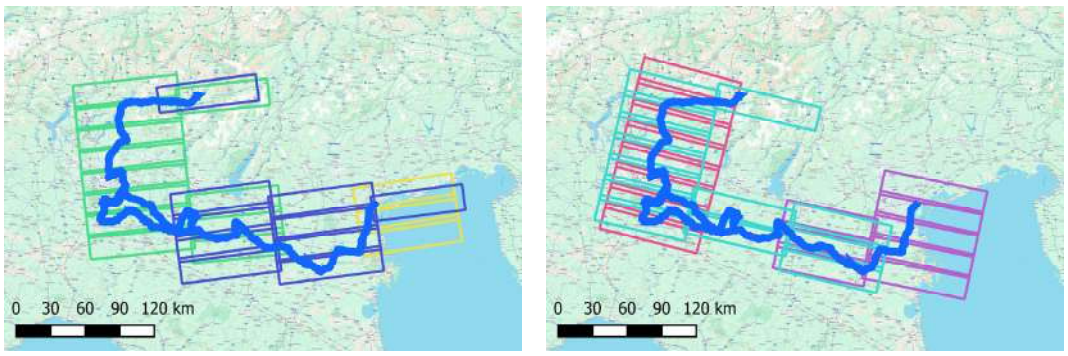

(**a**) (**b**)

Figure 7. Bursts individuated for downloading with EGMS-toolkit for (**a**) ascending orbit tracks, (**b**) descending orbit tracks. Each track indicated with different color.

After obtaining the raw EGMS files from multiple bursts and frames, the other three steps detailed in Section 2.2.1—Dataset Assembly, Data Export and Conversion, AOI Clipping—were carried out for the selected AOI. After all these operations, a clean dataset of PS points in the AOI consisting of about 2 million points for ascending orbit tracks and about 2.6 million points for descending orbit tracks was obtained.

It is worth noting that the proposed procedure uses EGMS data as an input without directly addressing the reliability of this data. Obviously, however, verifying the reliability of the input data is a necessary step. This can be achieved, for instance, through two main approaches: (i) the use of on-site sensor systems; (ii) comparison with data from other satellite constellations.

The first approach—on-site instrumentation—is undoubtedly the most accurate. In this context, the RETURN research project includes the installation of sensors on three selected bridges of the corridor used as case studies, which will enable future data validation and comparison.

As for the second approach, a comparison between EGMS data and CSK data is presented below. Figure 8 shows results obtained over the same area, representing one of the corridor bridges near Venice, using Sentinel-EGMS and CSK-SBAS dataset. The colors of the points indicate the mean annual velocity. The two datasets yield qualitatively comparable results; however, the much higher spatial resolution of the CSK imagery is evident, as reflected in the significantly greater density of measurement points over the same area.

It should also be noted that the EGMS has implemented standardized procedures to validate its results, both in terms of measurement point density and spatial coverage, as well as through comparisons with GNSS and other independent datasets, e.g., refs. [37,38].

The corridor selected as the AOI included the dataset of bridges accompanied—when available—by preliminary information such as structural typology, length, owner and other relevant attributes. The only geometrical information available was one point for each bridge, as visible in Figure 9. As explained in detail in Section 2.2.2, at least a line geometry representing each bridge is needed for the subsequent phases of the workflow. In this study the open dataset created by the OpenData SiciliaHub community based on OpenStreetMap data was used. In particular, the datasets for the Lombardia and Veneto regions were considered (see Figure 10) and the line features (representing bridges) along the corridor were selected. After this operation, the final dataset of bridges along the corridor consisted of approximately 480 entries, including bridges that cross or provide access to the corridor.

It is worth noting that a careful bridge-by-bridge check could be performed to further improve the dataset quality.

(**a**) (**b**)

Figure 8. View over same area of ascending (triangles pointing up) and descending (triangles pointing down) points for (**a**) EGMS dataset (product L2a); (**b**) CSK dataset.

Figure 9. Global view of whole corridor with different bridges indicated by green points.

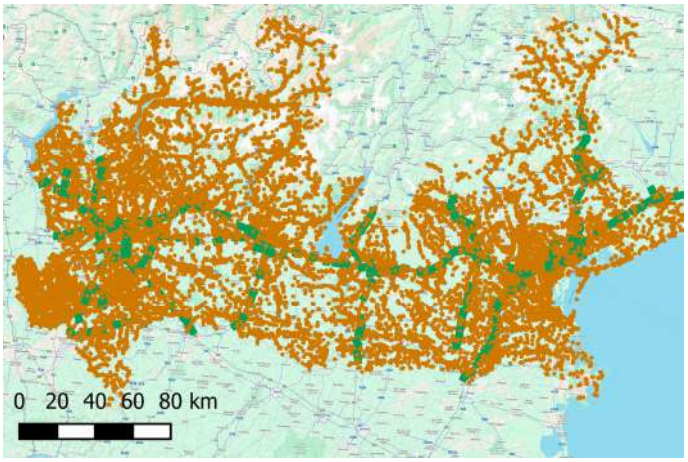

Figure 10. Dataset of bridges from OpenData SiciliaHub community based on OpenStreetMap data; green represents highway bridges.

4. Results

This section shows the results obtained by applying the proposed methodology to the case study area, highlighting the partial results obtained through the different steps of the proposed methodology described in Section 2, concerning the spatial join, deformation analysis, alert system and upscaling.

After the creation of bridge pixels and the operation of the spatial join, the dataset consisted of a total of 2999 pixels associated with 480 bridges. The number of pixels per bridge reached an average of 40.9 and a median of 13, with a minimum of 1 and a maximum of 193.

4.1. Spatial Join and Deformation Analysis

As previously shown in Figure 7, there is a significant overlap between satellite tracks. Consequently, each pixel may contain information from more than one ascending track (up to a maximum of two) and more than one descending track (also up to two). Table 1 reports the number of pixels corresponding to all possible combinations of ascending and descending track availability (i.e., zero ascending and zero descending, one ascending and zero descending, zero ascending and one descending, etc., up to two ascending and two descending).

Table 1. Number of pixels corresponding to all possible combinations of ascending and descending tracks.

Number of ASC, DES Tracks	Number of Possible Combinations	Number of Pixels
0, 0	0	342 (11.4%)
1, 0 or 0, 1	0	455 (15.2%)
2, 0 or 0,2	0	333 (11.1%)
1, 1	1	493 (16.4%)
1, 2 or 2, 1	2	1245 (41.5%)
2, 2	4	131 (4.4%)

It is worth noting that in approximately 10% of the pixels, no information is available from either ascending or descending orbits, thereby not permitting us to perform any further analysis. For around 15% of the pixels, information is available from only one orbit (either ascending or descending), while in another 10% the data is limited to only two tracks from the same orbit direction (i.e., two ascending or two descending). In these cases, it is not possible to reliably estimate both mean vertical and horizontal east–west velocity components; however, some of the flags discussed later in the paper may be still activated.

For approximately 16% of the pixels, exactly one ascending and one descending orbit are available, allowing for an unambiguous estimation of the mean vertical and horizontal east–west velocity components. In the remaining 45% of cases, the estimation of these components is ambiguous due to the presence of multiple possible ascending–descending pair combinations.

The distribution of pixel–track combinations is illustrated in Figure 11 for a specific bridge near Mantua (bridge POC2-ID6 in the POC2 corridor) considering three different time windows, 2015–2021, 2018–2022 and 2019–2023. It is worth noting that the distribution of available track combinations per pixel can vary over time. In particular, a portion of the bridge area becomes data-void in the 2019–2023 window. This is further emphasized in the zoomed-in view shown in Figure 12, which highlights a significant increase in the number of pixels lacking data points during the 2019–2023 period compared to the 2015–2021 window.

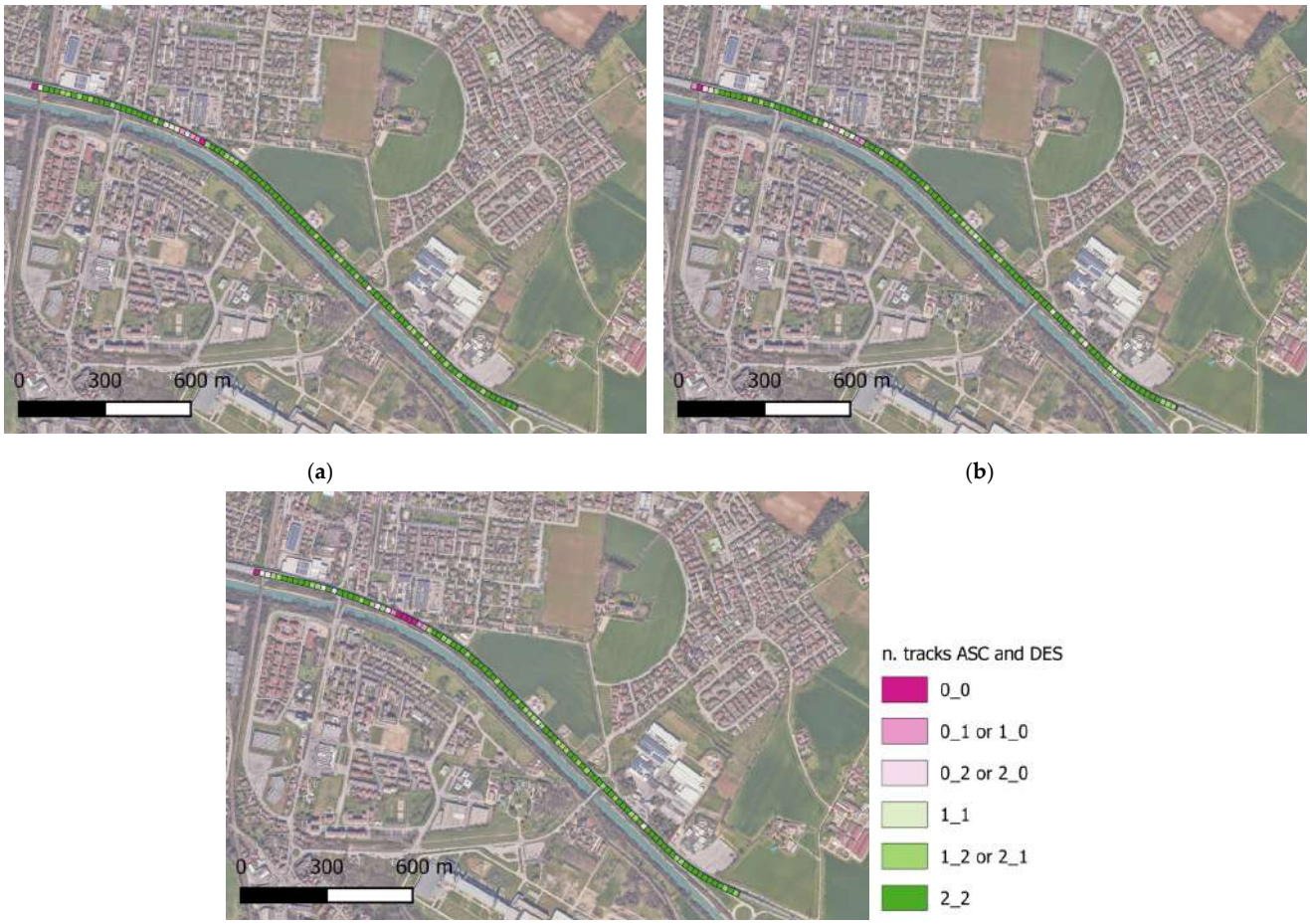

(**a**) (**b**)

(**c**)

Figure 11. Distribution of pixel–track combinations for specific bridge near Mantua (bridge POC2-ID6): (**a**) 2015–2021 time window; (**b**) 2018–2022 time window; (**c**) 2019–2023 time window.

(**a**) (**b**) (**c**)

Figure 12. Zoom-in on portion of bridge POC2-ID6: (**a**) 2015–2021 time window; (**b**) 2019–2023 time window; (**c**) legends.

To address this issue, a data reduction technique was proposed and applied in two distinct approaches, as described in Section 2.

According to the first approach (left side of the workflow depicted in Figure 1), all possible combinations of ascending and descending tracks are considered. To reduce the dataset, the maximum absolute values of the mean vertical and horizontal east–west

velocities are selected. This reduction can be performed either at the pixel level or at the bridge level.

Figure 13 schematically illustrates the pixel-by-pixel approach for bridge POC2-ID6, where different track combinations are selected for each pixel individually. An alternative approach is the bridge-by-bridge method, where the most frequently used track combination across the pixels of a given bridge is identified (in this example, 117A and 095D), and then uniformly applied to all the pixels of that bridge. Naturally, this may result in lower velocity values for some pixels compared to the pixel-by-pixel approach.

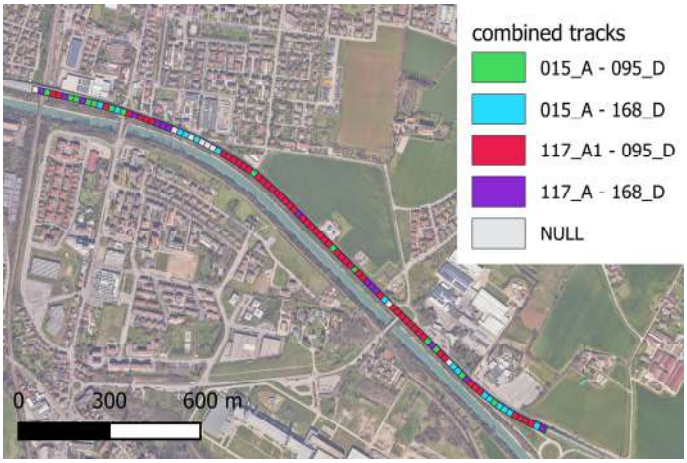

Figure 13. Different track combinations for each pixel for bridge POC2-ID6 for time window 2015–2021, obtained using pixel-by-pixel approach.

The final result, in terms of mean vertical velocity for each pixel across the three time windows, is shown in Figure 14 using a pixel-by-pixel approach.

To further investigate this outcome, in Figure 15 all four possible track combinations for the selected bridge (bridge POC2-ID6) are shown (top: ascending 015; bottom: ascending 117; left: descending 095; right: descending 168). Notable differences can be observed—particularly in the southeast area, which appears red in some combinations and blue in others. The differences between left and right (i.e., between descending tracks) appear to be more pronounced than those between top and bottom (i.e., between ascending tracks), suggesting that the variation in measurements could mainly have been introduced by the descending tracks.

This observation is further supported by Figure 16, which presents pair plots for the same bridge pixels for the mean vertical and horizontal east–west velocities.

In the second approach to data reduction, the selection of one ascending and one descending track is performed prior to the combination step. As with the previous method, this selection can be performed either on a pixel-by-pixel basis or on a bridge-by-bridge basis.

By evaluating the temporal coherence and the number of PSs available in each pixel, a selection metric QI can be defined as follows:

$$QI = w_\gamma \cdot \gamma + w_n \cdot n_p \tag{8}$$

where γ represents temporal coherence, n_p is the number of points in the considered pixel and w_γ and w_n are weighting factors. In this work the values assumed are w_γ = 1.0 and w_n= 0.25 to account for the ratio between the area of the analysis cell (20 × 20 = 400 m^2) and the nominal area of the satellite pixel (5 × 20 = 100 m^2).

Figure 17 illustrates, for each pixel, the selected track combination based on the metric defined by Equation (1).

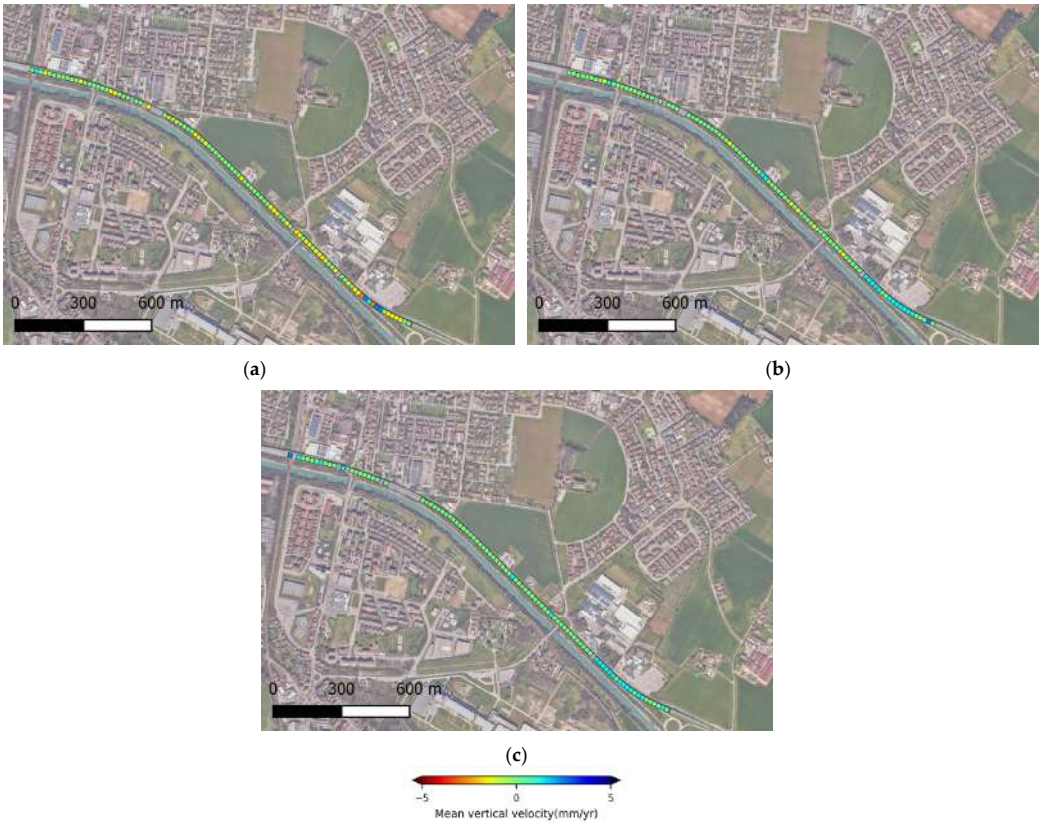

Figure 14. Mean vertical velocity for each pixel for bridge POC2-ID6 obtained using pixel-by-pixel approach across three time windows: (**a**) 2015–2021 time window; (**b**) 2018–2022 time window; (**c**) 2019–2023 time window.

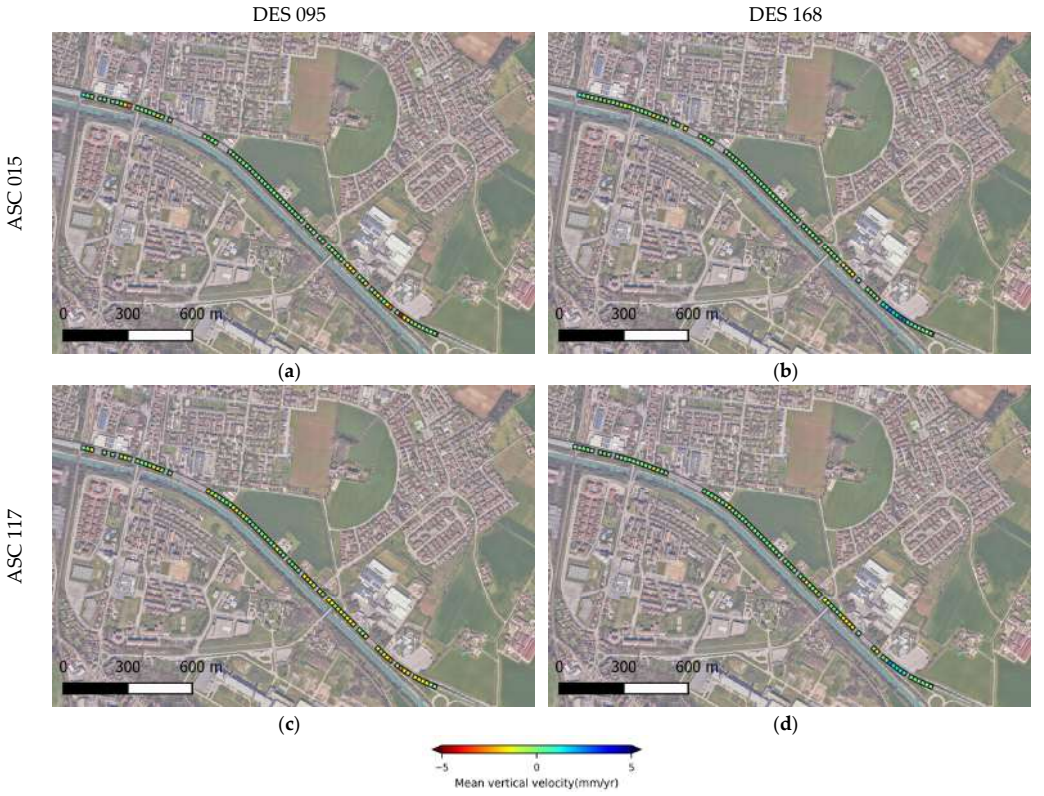

Figure 15. Four possible track combinations for bridge POC2-ID6 for time window 2015–2021: (**a**) ascending 015–descending 095; (**b**) ascending 015–descending 168; (**c**) ascending 117–descending 095; (**d**) ascending 117–descending 168.

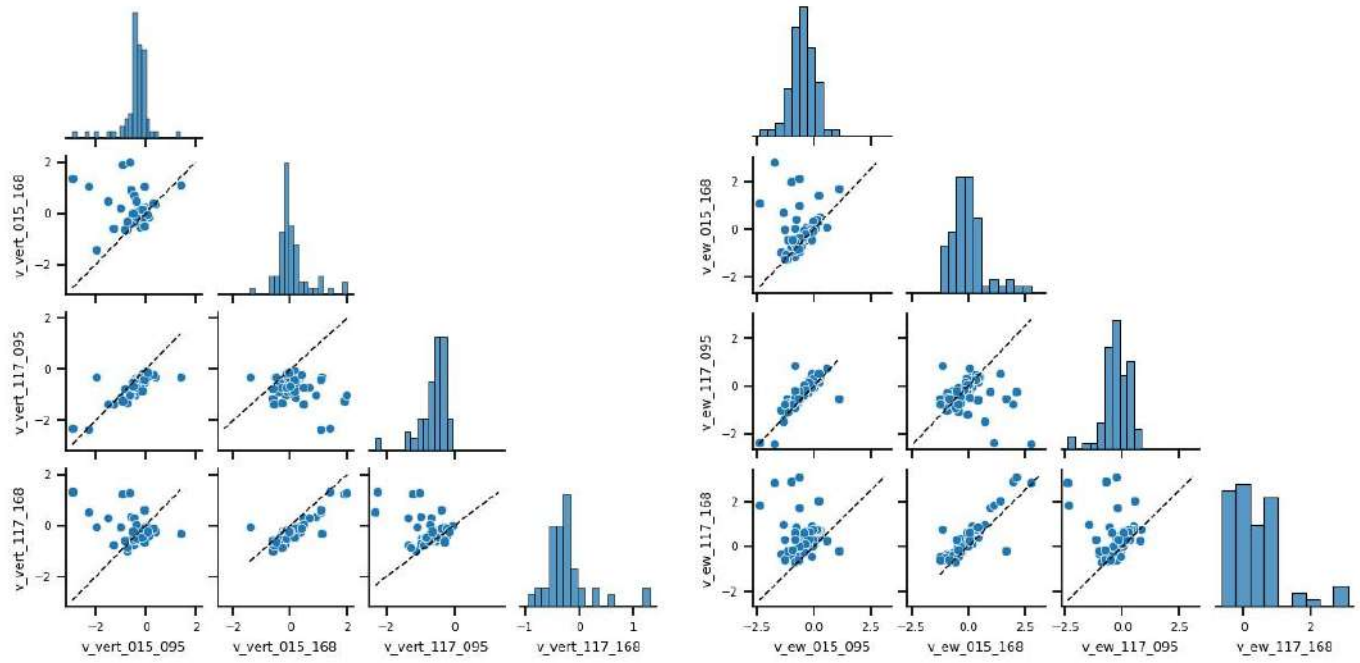

(**a**) (**b**)

Figure 16. Pair plots for pixels of bridge POC2-ID6 using different tracks available: (**a**) mean vertical velocity; (**b**) mean horizontal east–west velocity.

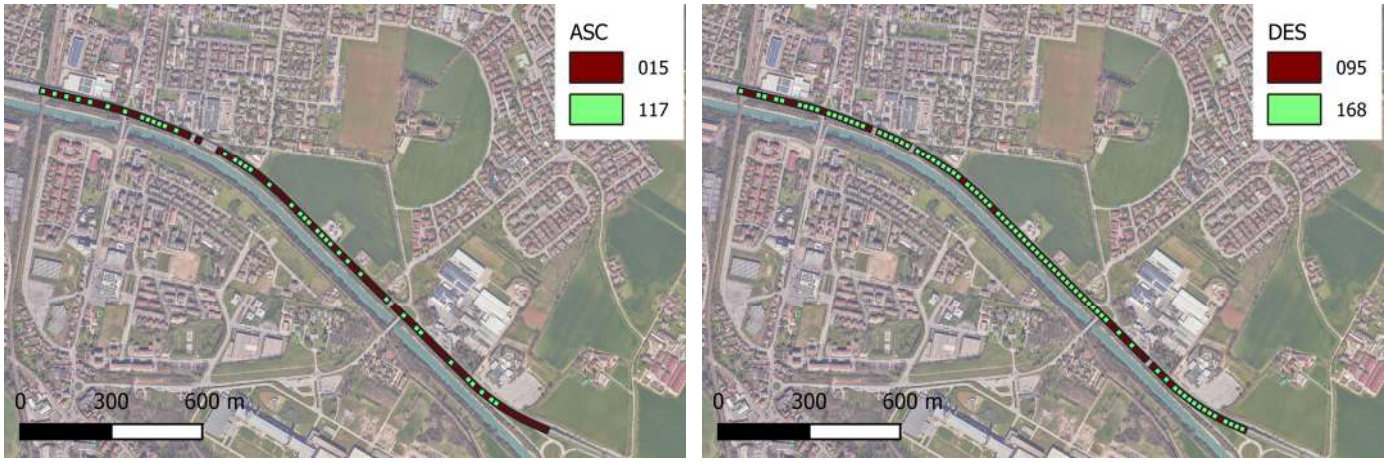

(**a**) (**b**)

Figure 17. Track combination for each pixel of bridge POC2-ID6 according to metric defined by Equation (1): (**a**) ascending tracks; (**b**) descending tracks.

Table 2 reports, for each track and orbit combination, the number of pixels for which each geometry was selected. It is possible to observe that most pixels exhibit better metrics for descending track 168 over 021, and similarly, for ascending acquisitions, track 015 outperforms track 117.

By applying the selection at the bridge level, tracks 015 (ascending) and 168 (descending) are chosen, thereby reducing the dataset to a single ascending–descending pair. The mean vertical and horizontal east–west velocity components computed using these two orbits correspond to the results shown in Figure 15b. These are also presented numerically in Figure 18. A slight mismatch between the two approaches can be observed for bridge POC2-ID6.

Table 2. Number of pixels for each track and orbit combination.

Track and Orbit Combination	Number of Pixels
015 (A)	59
117 (A)	40
095 (D)	21
168 (D)	80

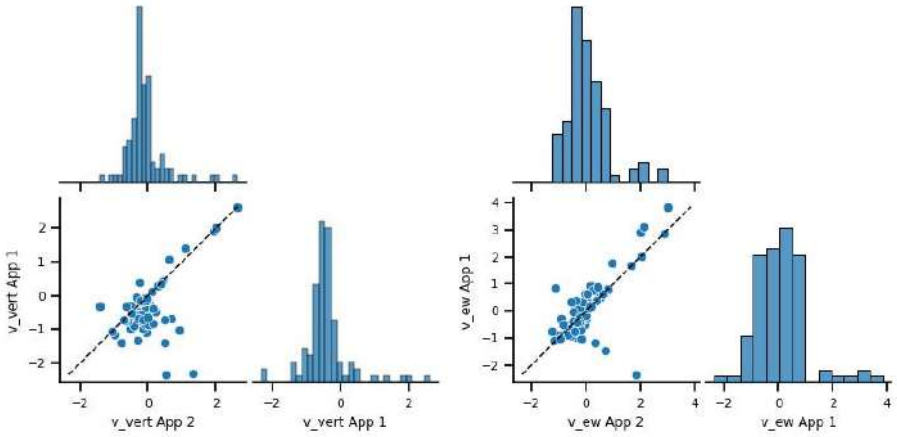

(**a**) (**b**)

Figure 18. Pair plots comparing velocities computed with approach 1 (pixel-by-pixel strategy) and with approach 2 (bridge-by-bridge strategy): (**a**) mean vertical velocity; (**b**) mean east–west velocity.

The main difference lies in the final combination of tracks selected. For example, with reference to Figure 19, consider the orange pixel near the light blue area in approach 1 (left) compared to the green pixel in the same location under approach 2 (right), marked by a purple circle. In approach 1, tracks 117 (ascending) and 168 (descending) are combined, as they yield the highest absolute value of mean vertical velocity. In contrast, approach 2 considers the quality of the available tracks. In this case, descending track 095 has a much lower quality index (QI = 0.74) compared to track 168 (QI = 1.93).

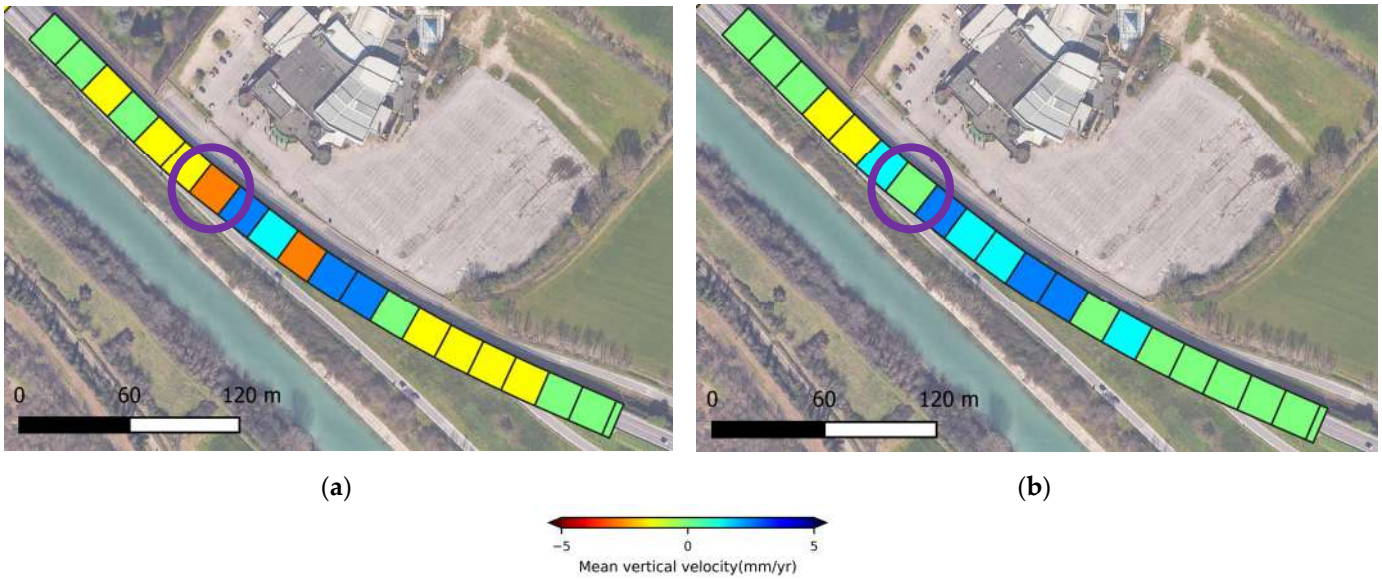

(**a**) (**b**)

Figure 19. Mean vertical velocity for different pixels in portion of bridge POC2-ID6: (**a**) approach 1; (**b**) approach 2. The purple circle indicates a pixel with significant difference between the two approaches.

This discrepancy is attributed to both the average temporal coherence (0.49 for track 095 vs. 0.68 for track 168) and the number of Persistent Scatterer (PS) points available (only one for track 095 versus five for track 168, see the pixels marked by a purple circle in Figure 20), making the measurement from track 168 significantly more robust.

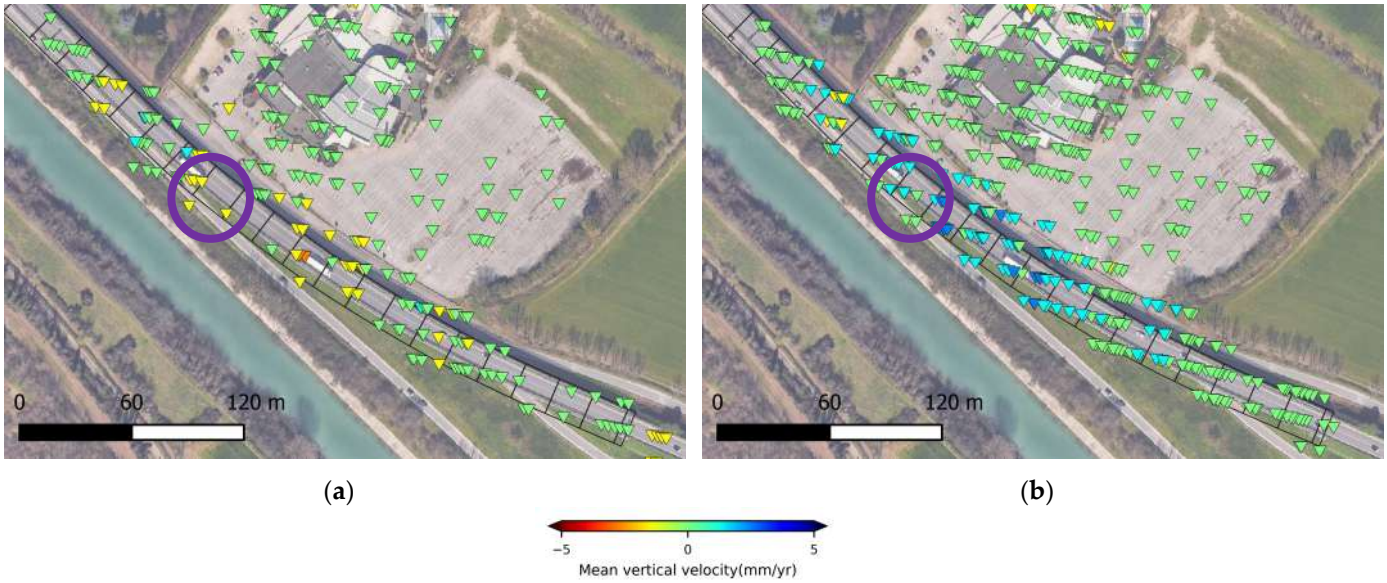

Figure 20. Portion of bridge POC2-ID6 with PSs colored based on mean displacement velocity: (**a**) descending track 095; (**b**) descending track 168. The purple circle indicates a pixel with significant difference between the two approaches.

4.2. Alert System and Upscaling

The following set of multi-criteria flags are activated for each pixel as part of the alert system:

1. A mean vertical velocity higher than a threshold of 4 mm/yr;
2. A mean horizontal velocity higher than a threshold of 4 mm/yr;
3. An ascending mean velocity along the LOS higher than a threshold of 4 mm/yr;
4. A descending mean velocity along the LOS higher than a threshold of 4 mm/yr;
5. Variation with respect to the previous time window larger than 100% for each of the above mentioned data points.

The third and fourth criteria are particularly relevant for pixels where only one orbit (ascending or descending) is available, which prevents the calculation of the vertical and east–west mean velocity components. The last criterion highlights whether significant differences have emerged since the previous EGMS release. It is worth noting that the threshold selected for criteria 1–4 (expressed in mm/years) does not directly affect the last criterion. Specifically, regarding this last criterion, the proposed value of 100% is not based on statistical considerations but is intended only as a trial value for testing the procedure.

Clearly, a proper calibration of all the proposed threshold values will be necessary for the assessment of individual bridges. This calibration can be performed, for example, once on-site sensor data become available from the monitoring systems that will be installed in the near future on three selected bridges along the corridor.

Additionally, especially when the velocities are low, the percentage difference can be very high even when the absolute value of the velocity is limited. Therefore, it may be helpful to set a velocity threshold below which the activation of the last flag is disregarded: in the proposed application the last flag is not applied when the velocity is below 0.5 mm/yr.

Specific threshold values can be selected based on the structural typology (e.g., slender vs. stiff bridges) following more detailed analyses. However, this aspect is not addressed in the present work, as the focus is primarily on illustrating the methodology rather than on calibrating thresholds for individual cases. Accordingly, the proposed thresholds should be considered as preliminary and illustrative suggestions. Nevertheless, modifying the threshold does not compromise the validity of the proposed methodology, which remains flexible and adaptable to different structural configurations and performance criteria. In this work, a value of 4 mm/yr was selected.

It is worth noting that the aim of the proposed procedure is to analyze satellite data on a large scale, to provide a prioritized list of bridges. The results do not directly identify bridges that have suffered damage, but rather those that should be highlighted for further investigation. This approach is intended to support a comparative, not absolute, evaluation, assuming the consistent application of the methodology across all bridges.

As mentioned in Section 2.4, to enhance the robustness of the alert system a statistical measure is included. In particular, the SEM for the ascending and descending mean velocities together with the uncertainty propagation for mean vertical and east–west components are computed.

As an example, Figure 21 shows the mean vertical velocities with the associated uncertainties obtained by applying approach 2 for combination and data reduction along bridge POC-ID6 for the three time windows available. A similar plot is shown in Figure 22 for the mean east–west velocity.

According to the proposed procedure, a flag is triggered when either the mean vertical velocity or the mean east–west velocity exceeds a fixed threshold (e.g., 4 mm/yr in this application). This condition can be evaluated either by considering only the mean values or by incorporating the uncertainty in their estimation. In the proposed example, the uncertainty was calculated using $\pm$ one standard deviation, which corresponds to approximately a 68% confidence interval. This implies that the flag is activated when there is more than a 156% probability that the true mean velocity exceeds the threshold.

As for Figures 21 and 22, it is possible to observe that the uncertainty in time window 2015–2021 is significantly smaller than the two newer time windows. This may be attributed to the larger number of images available for the first time window, which covers two additional years compared to the more recent ones. Indeed Figure 23 shows the standard deviation of velocity provided by the EGMS for POC2-ID6 across the different tracks and the three time windows. It is evident that the standard deviation is significantly higher for all the tracks in the two most recent time windows. Consequently, the SEM is also significantly higher in these recent time windows, leading to an increase in the propagated uncertainty. Furthermore, it is possible to observe that, in general, the central portion of the bridge is stable for all the time windows, indicating a certain stability in the whole period of 2015–2023; the right portion of the bridge shows some uplift and east-bound velocities, with larger values in the time window 2015–2021 that tend to reduce moving towards the subsequent time windows. Finally, it is possible to observe that in the last time window the left portion of the bridge shows an increased uplift and east-bound velocity.

This error evaluation improves the flagging process by taking into account measurement uncertainty rather than relying only on the mean value exceeding a threshold.

Therefore, looking for instance at Figures 21 and 22, the flag will be activated on those pixels for which the error bar is outside the threshold (see the left portion of the bridge).

With these flag criteria, the activated flags for the bridge POC-ID6 are depicted in Figure 24. It is possible to see that in one pixel the mean vertical velocity and the mean east–west velocity are above the selected threshold of 4 mm/yr (as was evident also from Figures 21 and 22). For one pixel the mean velocity for the ascending orbit is above the

selected threshold, while the mean velocity for the descending orbit is above the threshold for three pixels. Several pixels instead show a percentage difference between two adjacent time windows higher than the selected threshold of 100%.

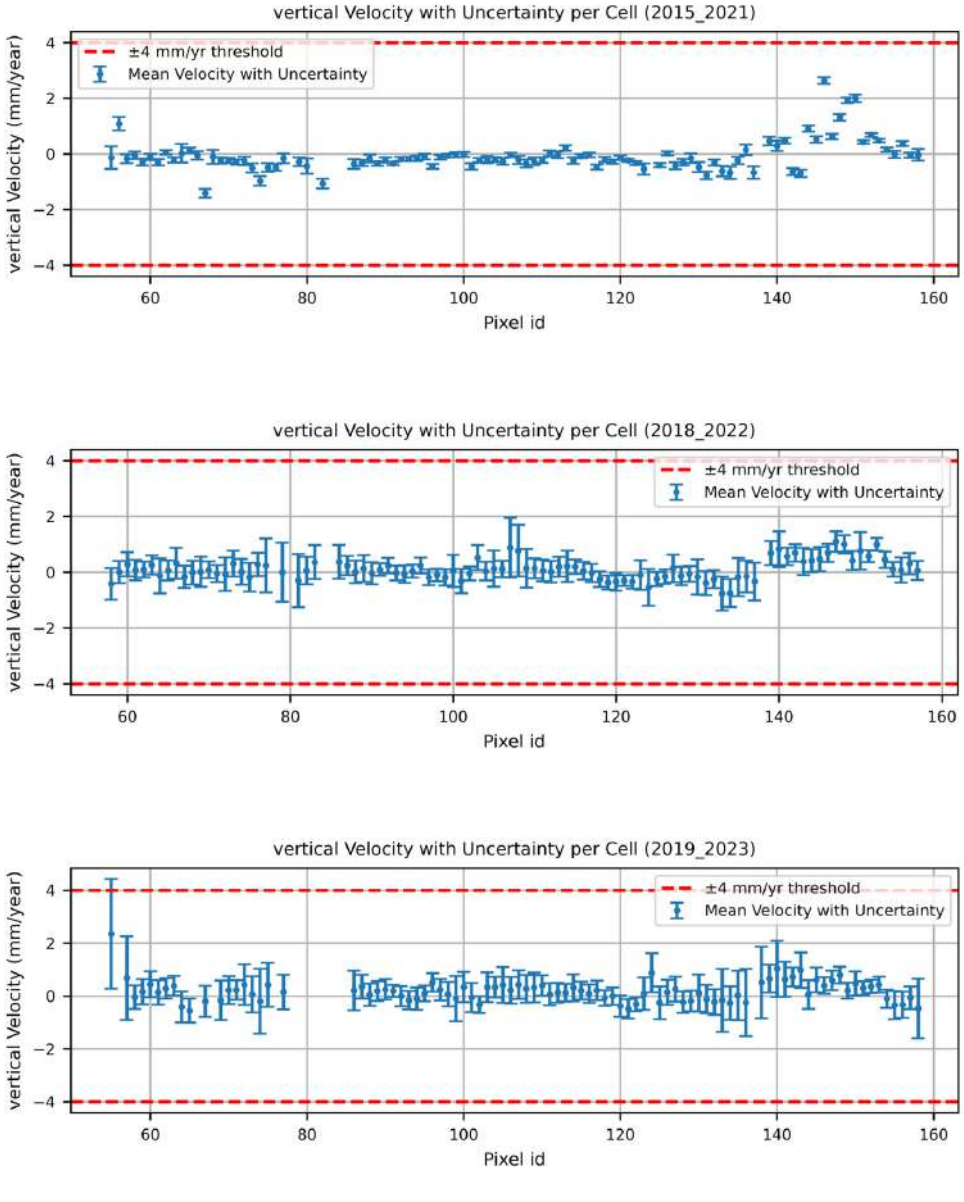

Figure 21. Mean vertical velocity for POC2-ID6 bridge with approach 2 across three time windows: (**a**) 2015–2021 time window; (**b**) 2018–2022 time window; (**c**) 2019–2023 time window.

As explained in Section 2.4, in order to help stakeholders by providing a clear and concise overview of the condition of the bridges within the relevant network, an upscaling procedure is applied: a bridge is flagged if at least one of its pixels has an active warning flag. As an example of this result, obtained by applying approach 2 for combination and data reduction, Figure 25 shows the whole AOI of the corridor, indicating which bridges (shown in red) are characterized by having at least one pixel with an activated flag. In total, 199 bridges have an activated flag. All the 199 bridges activated a flag because in at least one pixel a significant difference (higher than 100%) was detected between the time windows of 2015–2021 and 2018–2022. If one disregards the flags related to differences between adjacent time windows, only 65 bridges show the activation of a flag (due to velocities along the LOS for descending orbit higher than 4 mm/year). Considering vertical

and east–west component flags, only 31 bridges show a vertical and/or east–west velocity higher than 4 mm/yr.

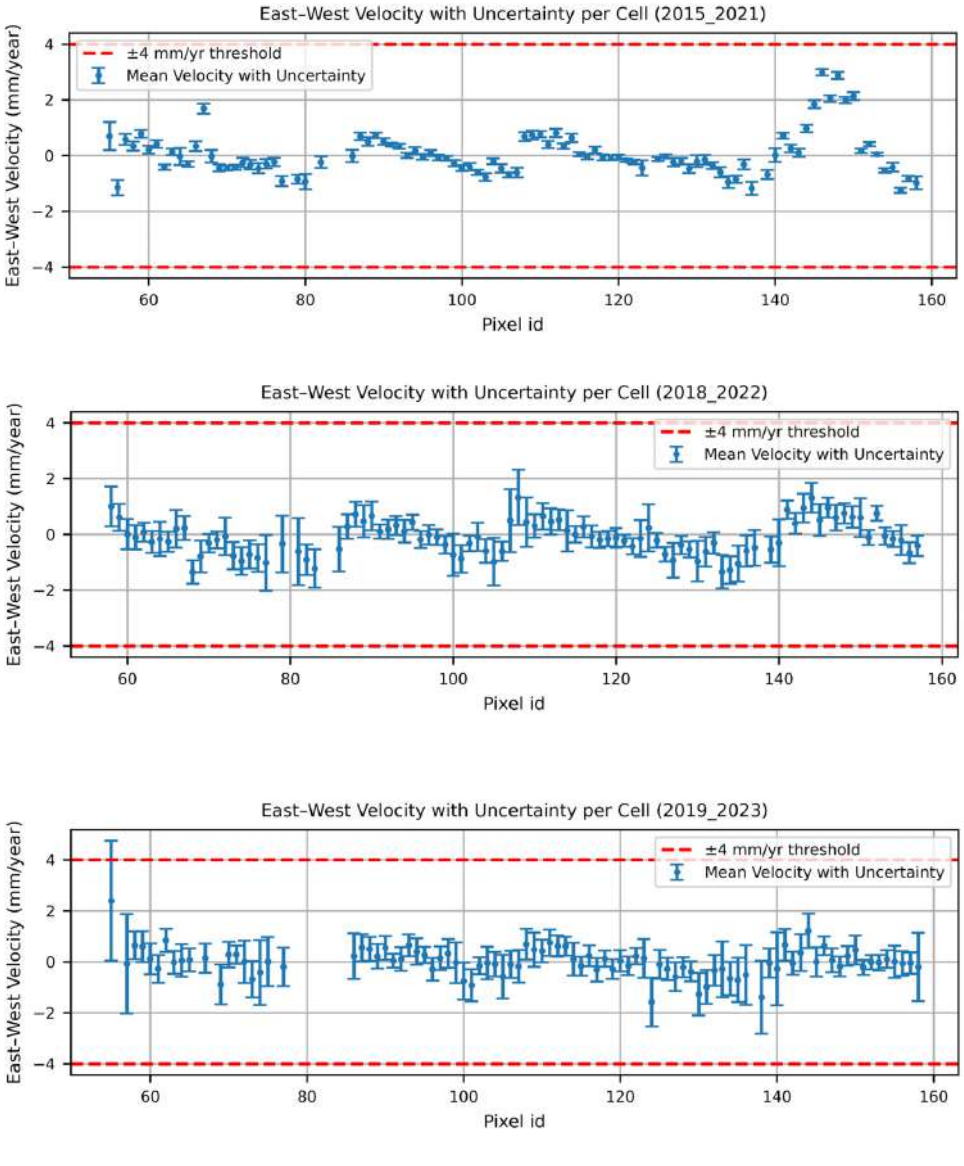

Figure 22. Mean east–west velocity for POC2-ID6 bridge with approach 2 across three time windows: (**a**) 2015–2021 time window; (**b**) 2018–2022 time window; (**c**) 2019–2023 time window.

For comparison, if one considers 2 mm/yr as the threshold, 199 bridges still activate a flag because of the significant differences between adjacent time windows. Disregarding this last flag, 261 bridges have a flag activated because of their velocity along the LOS for descending orbit is higher than 2 mm/yr. Considering instead only vertical and east–west component flags, 191 bridges activate a flag.

A flag should not be interpreted as direct evidence of structural damage, but as an indication that further bridge-level assessment is needed, ideally combining satellite observations with in situ data.

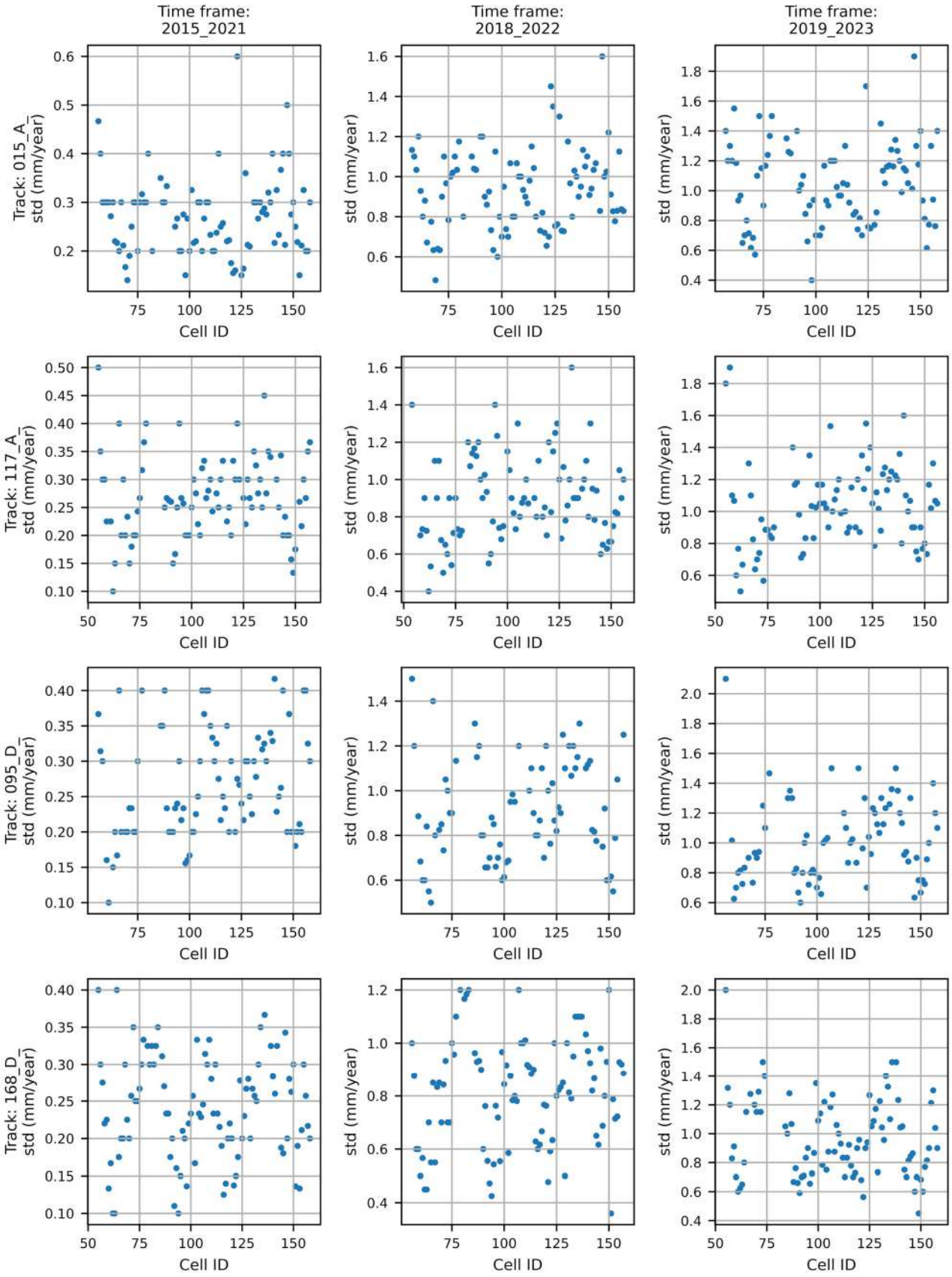

Figure 23. Standard deviation of velocity provided by EGMS for POC2-ID6 for different tracks and three time windows.

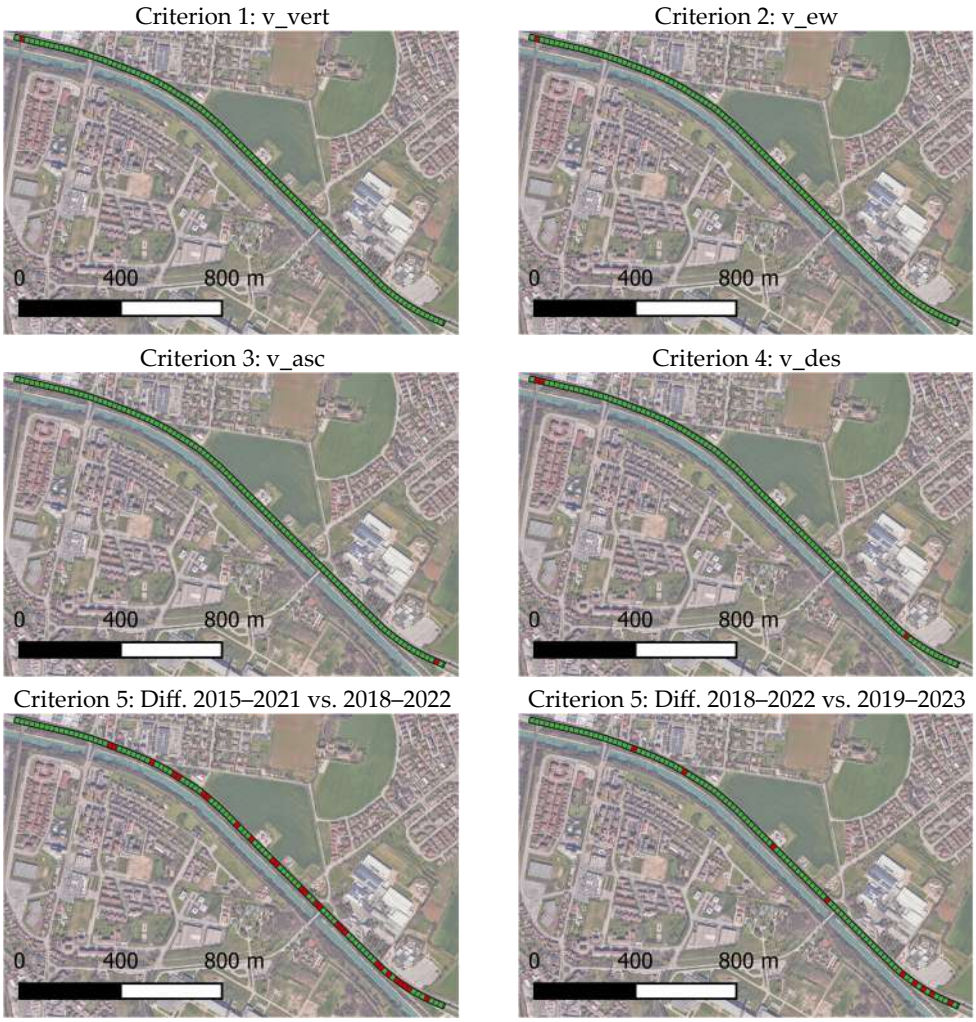

Figure 24. Flags activated for each pixel of bridge POC-ID6: green indicates flag not raised, while red indicates flag raised.

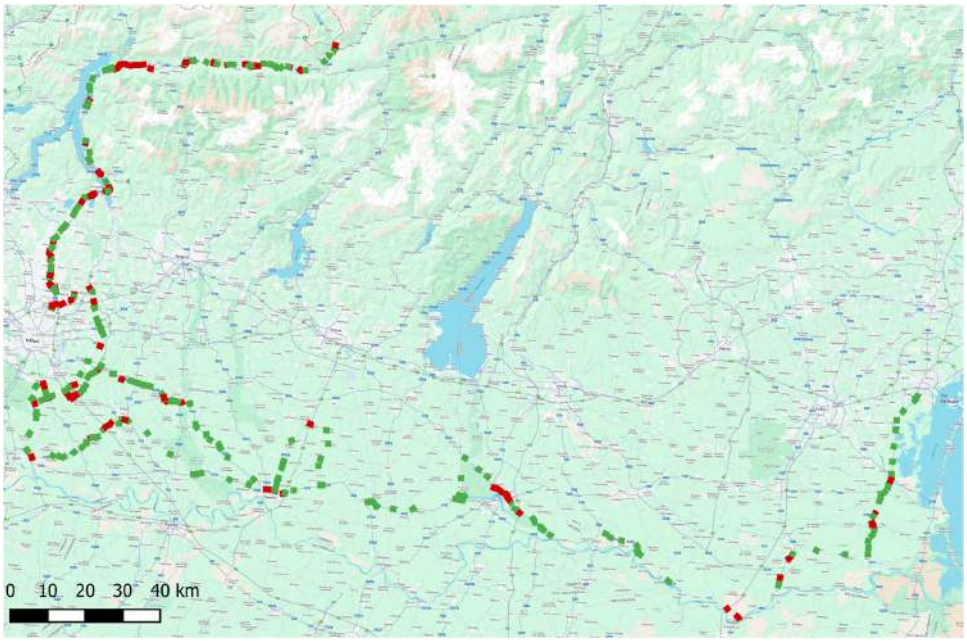

Figure 25. A view of the whole AOI: The green bridges indicate bridges with no flags activated, while the red bridges indicate those that have at least one pixel with an activated flag.

5. Discussion

The results obtained through the proposed methodology highlight both the potential and the inherent complexities of leveraging EGMS data for large-scale bridge monitoring. A significant finding relates to the heterogeneous availability of satellite tracks across the study area. While approximately 16% of the pixels benefit from a complete ascending–descending pair enabling reliable 2D velocity decomposition, nearly half of the dataset presents ambiguous configurations, where multiple track combinations complicate the derivation of consistent deformation parameters. This heterogeneity emphasizes the importance of robust data reduction strategies capable of adapting to varying data quality and coverage.

The comparison between the two proposed data reduction approaches—max-absolute (Approach 1) versus quality-informed (Approach 2)—reveals fundamental trade-offs between sensitivity and reliability. The pixel-level selection in Approach 1, while effective at identifying extreme velocity values, may be more susceptible to artifacts arising from low-coherence or sparsely sampled tracks. Approach 2, by incorporating a quality index that accounts for temporal coherence and the number of PS points, prioritizes data robustness. The observed differences in selected tracks and resultant velocities for the same pixels (e.g., Figure 19) underscore the critical role of quality-driven data processing. Ordinary Least Squares, or better Weighted Least Squares can be explored as a third approach for considering all the available information for the different tracks while weighting them with their quality measure.

The temporal component of the analysis performed also warrants discussion. The reduction in data quality observed in the most recent time windows (2018–2022 and particularly 2019–2023), as evidenced by increased standard deviations and *SEM*s, probably stems from the reduced number of acquisitions in those periods respect to the first time window (i.e., 2015-2021) that is characterized roughly by 40% more radar images. This affects both the reliability of velocity estimates and the uncertainty bounds used in the alerting mechanism.

The alert system itself proves effective in translating raw satellite data into structured, interpretable signals for decision-makers. In particular, the inclusion of both absolute velocity thresholds and temporal variation criteria provides a nuanced framework capable of flagging both persistent and emerging anomalies. Another critical observation relates to the spatial distribution of flagged pixels. As an example, in bridge POC2-ID6, certain sections exhibited localized uplift or east-bound motion that seems to be evolved across the time windows. This kind of intra-bridge spatial variation, when consistently detected, can inform targeted inspections and even structural assessment if integrated with engineering models.

The results from the upscaling procedure confirm the practicality of this method for prioritizing interventions. The significant number of bridges flagged when only temporal variation is considered (199 bridges), compared to those flagged based on absolute displacement thresholds (31 bridges), suggests that change detection can reveal early-stage trends that absolute thresholds might miss, even if care should be paid in selecting a significant change of velocity in time respect to unsignificant noise.

6. Conclusions

This study presents a semi-automatic methodology for the large-scale monitoring of bridges using MT-DInSAR data, with a focus on practical implementation for infrastructure management. By integrating satellite-derived measurements with enhanced geospatial representations of bridge assets, the proposed approach enables a systematic evaluation of deformation patterns at the bridge scale. The methodology includes key phases such

as spatial data enrichment, PS-InSAR data processing, component-wise velocity estimation and an alert system incorporating statistical uncertainty, which together support the early detection of potential structural issues. Applied to the transport corridor between Tirano and Marghera, designated for exceptional transport operations, studied within the NRRP RETURN project, the approach demonstrates its ability to identify bridges exhibiting anomalous displacement behavior. While the defined thresholds serve as illustrative examples, the framework remains flexible and can be adapted to different structural typologies and monitoring requirements. In particular, the possibility of using different threshold values depending on the type of bridge should be considered. Overall, this methodology provides a scalable tool that enhances current practices in bridge health monitoring, offering valuable support for data-driven maintenance planning and risk mitigation.

Author Contributions: Conceptualization, methodology, writing—original draft preparation, validation, writing—review and editing, D.A.T. and A.S.; investigation, software, formal analysis, visualization, data curation, D.A.T.; supervision, project administration, funding acquisition, A.S. All authors have read and agreed to the published version of the manuscript.

Funding: This research was carried out within the RETURN Extended Partnership and received funding from the European Union Next-GenerationEU project (National Recovery and Resilience Plan—NRRP, Mission 4, Component 2, Investment 1.3—D.D. 1243 2/8/2022, PE0000005).

Data Availability Statement: The results of the analyses carried out on the existing dataset are not publicly available due to confidentiality restrictions, as the research project funding this study is still ongoing.

Conflicts of Interest: The authors declare no conflicts of interest.

References

1. Ferretti, A.; Prati, C.; Rocca, F. Permanent Scatterers in SAR Interferometry. *IEEE Trans. Geosci. Remote Sens.* **2001**, *39*, 8–20. [CrossRef]
2. Ferretti, A.; Fumagalli, A.; Novali, F.; Prati, C.; Rocca, F.; Rucci, A. A New Algorithm for Processing Interferometric Data-Stacks: SqueeSAR. *IEEE Trans. Geosci. Remote Sens.* **2011**, *49*, 3460–3470. [CrossRef]
3. Berardino, P.; Fornaro, G.; Lanari, R.; Sansosti, E. A New Algorithm for Surface Deformation Monitoring Based on Small Baseline Differential SAR Interferograms. *IEEE Trans. Geosci. Remote Sens.* **2002**, *40*, 2375–2383. [CrossRef]
4. Perissin, D.; Wang, T. Repeat-Pass SAR Interferometry with Partially Coherent Targets. *IEEE Trans. Geosci. Remote Sens.* **2012**, *50*, 271–280. [CrossRef]
5. Milillo, P.; Giardina, G.; Perissin, D.; Milillo, G.; Coletta, A.; Terranova, C. Pre-Collapse Space Geodetic Observations of Critical Infrastructure: The Morandi Bridge, Genoa, Italy. *Remote Sens.* **2019**, *11*, 1403. [CrossRef]
6. Infante, D.; Di Martire, D.; Calcaterra, D.; Miele, P.; Scotto di Santolo, A.; Ramondini, M. Integrated Procedure for Monitoring and Assessment of Linear Infrastructures Safety (I-Pro MONALISA) Affected by Slope Instability. *Appl. Sci.* **2019**, *9*, 5535. [CrossRef]
7. Tonelli, D.; Caspani, V.F.; Valentini, A.; Rocca, A.; Torboli, R.; Vitti, A.; Perissin, D.; Zonta, D. Interpretation of Bridge Health Monitoring Data from Satellite InSAR Technology. *Remote Sens.* **2023**, *15*, 5242. [CrossRef]
8. Chang, L.; Dollevoet, R.P.B.J.; Hanssen, R.F. Nationwide Railway Monitoring Using Satellite SAR Interferometry. *IEEE J. Sel. Top. Appl. Earth Obs. Remote Sens.* **2017**, *10*, 596–604. [CrossRef]
9. Macchiarulo, V.; Milillo, P.; Blenkinsopp, C.; Giardina, G. Monitoring Deformations of Infrastructure Networks: A Fully Automated GIS Integration and Analysis of InSAR Time-Series. *Struct. Health Monit.* **2022**, *21*, 1849–1878. [CrossRef]
10. Selvakumaran, S.; Plank, S.; Geiß, C.; Rossi, C.; Middleton, C. Remote Monitoring to Predict Bridge Scour Failure Using Interferometric Synthetic Aperture Radar (InSAR) Stacking Techniques. *Int. J. Appl. Earth Obs. Geoinf.* **2018**, *73*, 463–470. [CrossRef]
11. Cusson, D.; Rossi, C.; Ozkan, I.F. Early Warning System for the Detection of Unexpected Bridge Displacements from Radar Satellite Data. *J. Civ. Struct. Health Monit.* **2021**, *11*, 189–204. [CrossRef]
12. Cusson, D.; Trischuk, K.; Hébert, D.; Hewus, G.; Gara, M.; Ghuman, P. Satellite-Based InSAR Monitoring of Highway Bridges: Validation Case Study on the North Channel Bridge in Ontario, Canada. *Transp. Res. Rec. J. Transp. Res. Board.* **2018**, *2672*, 76–86. [CrossRef]

13. Talledo, D.A.; Miano, A.; Bonano, M.; Di Carlo, F.; Lanari, R.; Manunta, M.; Meda, A.; Mele, A.; Prota, A.; Saetta, A.; et al. Satellite Radar Interferometry: Potential and Limitations for Structural Assessment and Monitoring. *J. Build. Eng.* **2022**, *46*, 103756. [CrossRef]
14. Jung, J.; Kim, D.; Palanisamy Vadivel, S.K.; Yun, S.-H. Long-Term Deflection Monitoring for Bridges Using X and C-Band Time-Series SAR Interferometry. *Remote Sens.* **2019**, *11*, 1258. [CrossRef]
15. Lazecky, M.; Hlavacova, I.; Bakon, M.; Sousa, J.J.; Perissin, D.; Patricio, G. Bridge Displacements Monitoring Using Space-Borne X-Band SAR Interferometry. *IEEE J. Sel. Top. Appl. Earth Obs. Remote Sens.* **2017**, *10*, 205–210. [CrossRef]
16. Markogiannaki, O.; Xu, H.; Chen, F.; Mitoulis, S.A.; Parcharidis, I. Monitoring of a Landmark Bridge Using SAR Interferometry Coupled with Engineering Data and Forensics. *Int. J. Remote Sens.* **2022**, *43*, 95–119. [CrossRef]
17. Farneti, E.; Cavalagli, N.; Costantini, M.; Trillo, F.; Minati, F.; Venanzi, I.; Ubertini, F. A Method for Structural Monitoring of Multispan Bridges Using Satellite InSAR Data with Uncertainty Quantification and its Pre-Collapse Application to the Albiano-Magra Bridge in Italy. *Struct. Health Monit.* **2023**, *22*, 353–371. [CrossRef]
18. Miano, A.; Mele, A.; Silla, M.; Bonano, M.; Striano, P.; Lanari, R.; Di Ludovico, M.; Prota, A. Space-Borne DInSAR Measurements Exploitation for Risk Classification of Bridge Networks. *J. Civ. Struct. Health Monit.* **2024**, *15*, 731–744. [CrossRef]
19. Ignatenko, V.; Laurila, P.; Radius, A.; Lamentowski, L.; Antropov, O.; Muff, D. ICEYE Microsatellite SAR Constellation Status Update: Evaluation of First Commercial Imaging Modes. In Proceedings of the 2020 IEEE International Geoscience and Remote Sensing Symposium, Waikoloa, HI, USA, 26 September–2 October 2020; pp. 3581–3584. [CrossRef]
20. Stringham, C.; Farquharson, G.; Castelletti, D.; Quist, E.; Riggi, L.; Eddy, D.; Soenen, S. The Capella X-Band SAR Constellation for Rapid Imaging. In Proceedings of the IGARSS 2019—2019 IEEE International Geoscience and Remote Sensing Symposium, Yokohama, Japan, 28 July–2 August 2019; pp. 9248–9251. [CrossRef]
21. Macchiarulo, V.; Milillo, P.; Blenkinsopp, C.; Reale, C.; Giardina, G. Multi-Temporal InSAR for Transport Infrastructure Monitoring: Recent Trends and Challenges. *Proc. Inst. Civ. Eng. Bridge Eng.* **2023**, *176*, 92–117. [CrossRef]
22. Manconi, A.; Bühler, Y.; Stoffel, A.; Gaume, J.; Zhang, Q.; Tolpekin, V. Brief Communication: Monitoring Impending Slope Failure with Very High-Resolution Spaceborne Synthetic Aperture Radar. *Nat. Hazards Earth Syst. Sci.* **2024**, *24*, 3833–3839. [CrossRef]
23. Castelletti, D.; Farquharson, G.; Brown, J.; De, S.; Yague-Martinez, N.; Stringham, C.; Yalla, G.; Villarreal, A. Capella Space VHR SAR Constellation: Advanced Tasking Patterns and Future Capabilities. In Proceedings of the IGARSS 2022—2022 IEEE International Geoscience and Remote Sensing Symposium, Kuala Lumpur, Malaysia, 17–22 July 2022; pp. 4137–4140. [CrossRef]
24. Banic, M.; Ristic-Durrant, D.; Madic, M.; Klapper, A.; Trifunovic, M.; Simonovic, M.; Fischer, S. The Use of Earth Observation Data for Railway Infrastructure Monitoring—A Review. *Infrastructures* **2025**, *10*, 66. [CrossRef]
25. Wang, J.; Lu, Z.; Bekaert, D.; Marshak, C.; Govorcin, M.; Sangha, S.; Kennedy, J.; Gregg, P. Along-Arc Volcanism in the Western and Central Aleutian from 2015 to 2021 Revealed by Cloud-Based InSAR Processing. *Geophys. Res. Lett.* **2023**, *50*, e2023GL106323. [CrossRef]
26. Talledo, D.A.; Miano, A.; Di Carlo, F.; Bonano, M.; Mele, A.; Stella, A.; Lanari, R.; Meda, A.; Prota, A.; Saetta, A. Algorithms for Large-Scale Quasi-Real Time Monitoring of Architectural and Cultural Heritage Based on MT-DInSAR Data. *Lect. Notes Civ. Eng.* **2023**, *432*, 727–735. [CrossRef]
27. Abbozzo, A.; Zani, G.; Di Prisco, M. A New Approach to Improve Safe Exceptional Transpor-Tation: A Proof of Concept in the Framework of NRRP. In Proceedings of the 15th fib International PhD Symposium in Civil Engineering 2024, Budapest, Hungary, 28–30 August 2024; p. 457464.
28. Costantini, M.; Minati, F.; Trillo, F.; Ferretti, A.; Novali, F.; Passera, E.; Dehls, J.; Larsen, Y.; Marinkovic, P.; Eineder, M.; et al. European Ground Motion Service (EGMS). In Proceedings of the 2021 IEEE International Geoscience and Remote Sensing Symposium, Brussels, Belgium, 11–16 July 2021; pp. 3293–3296. [CrossRef]
29. Crosetto, M.; Solari, L.; Balasis-Levinsen, J.; Bateson, L.; Casagli, N.; Frei, M.; Oyen, A.; Moldestad, D.A.; Mróz, M. Deformation Monitoring at European Scale: The Copernicus Ground Motion Service. *Int. Arch. Photogramm. Remote Sens. Spat. Inf. Sci.* **2021**, *XLIII-B3-2021*, 141–146. [CrossRef]
30. Crosetto, M.; Solari, L.; Mróz, M.; Balasis-Levinsen, J.; Casagli, N.; Frei, M.; Oyen, A.; Moldestad, D.A.; Bateson, L.; Guerrieri, L.; et al. The Evolution of Wide-Area DInSAR: From Regional and National Services to the European Ground Motion Service. *Remote Sens.* **2020**, *12*, 2043. [CrossRef]
31. Copernicus Webinar "How to Use EGMS Data". Questions and Answers, 13 May 2024. Available online: https://land.copernicus.eu/en/events/learn-to-use-and-interpret-the-european-ground-motion-service-data/q-a_egms_webinar_responses_130524.pdf/@@download/file (accessed on 7 April 2025).
32. Hrysiewicz, A.; Khoshlahjeh Azar, M.; Holohan, E.P. EGMS-Toolkit: A Set of Python Scripts for Improved Access to Datasets from the European Ground Motion Service. *Earth Sci. Inf.* **2024**, *17*, 3825–3837. [CrossRef]
33. Rouault, E.; Warmerdam, F.; Schwehr, K.; Kiselev, A.; Butler, H.; Łoskot, M.; Szekeres, T.; Tourigny, E.; Landa, M.; Miara, I.; et al. GDAL. Available online: https://gdal.org/en/stable/ (accessed on 10 May 2025).

34. OpenDataSicilia Github Repository to Maps of Bridges in Italy by Region. Available online: https://github.com/SiciliaHub/mappe/tree/gh-pages/pontieviadotti (accessed on 7 May 2025).
35. Bevington, P.R.; Robinson, D.K. *Data Reduction and Error Analysis for the Physical Sciences*, 3rd ed.; McGraw-Hill Publishing: New York, NY, USA, 2003; ISBN 0072472278.
36. Fuhrmann, T.; Garthwaite, M.C. Resolving Three-Dimensional Surface Motion with InSAR: Constraints from Multi-Geometry Data Fusion. *Remote Sens.* **2019**, *11*, 241. [CrossRef]
37. Vradi, A.; Sala, J.; Solari, L.; Balasis-Levinsen, J. Validating the European Ground Motion Service: An Assessment of Measurement Point Density. *Int. Arch. Photogramm. Remote Sens. Spat. Inf. Sci.* **2023**, *XLVIII-4/W7-2023*, 247–252. [CrossRef]
38. Koudogbo, F.; Vöge, M.; Martins, J.E.; Raucoules, D.; De Michelle, M.; Vecchiotti, F. *EGMS Validation Report: Third Update*; EEA: Copenhagen, Denmark, 2025.